Polymer Journal (2019) 51:109–130
https://doi.org/10.1038/s41428-018-0147-2

REVIEW

Hierarchically self-organized filler particles in polymers: cascade evolution of dissipative structures to ordered structures

Takeji Hashimoto[1] · Naoya Amino[2] · Shotaro Nishitsuji[3] · Mikihito Takenaka[4]

Received: 20 August 2018 / Revised: 21 September 2018 / Accepted: 25 September 2018 / Published online: 20 December 2018

Abstract

Self-organization in nonequilibrium systems is an important research topic in the physical sciences for understanding the formation of patterns or orders in various systems, including patterns in nature. In this study, we investigated the self-organization of nanoparticles dispersed in polymer melts under applied mechanical energy imposed to mixtures that are composed of a bulk of the particle powder and a bulk of the polymer melt. Using various scattering methods that enable the exploration of structures that exist over a length scale that spans from ~0.1 nm to ~20 μm, we elucidated that the self-organized particles had hierarchical structures with various hierarchical levels as follows: primary particles (PPs), aggregates of the PPs fused together, clusters of the aggregates, and partially interdigitating mass-fractal structures built up by the clusters. The structures of the cluster and the fractal structures depend on attractive interactions between the polymers and the aggregates in given mixing conditions. We propose that the self-organization is caused by cascade evolutions of various dissipative structures, which are involved in the following energy dissipation processes driven by the deformation and flow of polymers during the mixing process. Dissipation Process I involves the fracture and flow of the particle grains in the powder, within which particles are bonded by interparticle attractive forces in air; the outer surfaces of which are in contact with the polymer matrix via polymer–particle interaction. Dissipation Process II involves the initial formation of the clusters, in which the aggregates are bound by polymers and subsequent formation of the mass-fractal agglomerates of the clusters via the diffusion-limited cluster–cluster association in the polymer matrix. The cascade structure evolutions and applied energy dissipation invoke a cascade reduction of the free energy of systems toward a minimum driven by net attractive interactions between the particles and the polymers throughout Dissipation Processes I and II.

I. Introduction

Elucidation of the self-organization of nanoparticles (NPs) in polymer matrices in externally applied mechanical fields is an important research topic not only from the viewpoint of fundamental polymer physics and materials science but also from the viewpoints of fundamental physical science. The topic is relevant to universal problems regarding the pattern formation or self-organization of dissipative structures via fluctuations in nonequilibrium systems that open to external fields [1]. We define the dissipative structures as ordered structures that are formed in nonequilibrium systems in external fields: various dissipative structures may be formed in a cascade accompanied by cascade dissipation processes of energy imposed on given systems in given external fields.

In this paper, we focus on elucidating the self-organization of NPs that are developed in nanocomposites of rubber-like polymers and filler particles that have NPs as "primary" particles (average radius of 13 nm), as will be detailed later. We present a new concept that is based on our results published in ref [2]. and newly added results and analyses in this study.

✉ Takeji Hashimoto
hashi2@pearl.ocn.ne.jp

✉ Naoya Amino
naoya.amino@y-yokohama.com

[1] Kyoto University, Kyoto 606-8501, Japan
[2] The Yokohama Rubber Co., Ltd., Kanagawa 254-8601, Japan
[3] Yamagata University, Yamagata, Japan
[4] Kyoto University, Kyoto 611-0011, Japan

The external fields relevant to our systems are (1) a field applied to mix a bulk of rubbery polymers and that of powder of filler particles, (2) a field subsequently applied to press the mixtures into a sheet, and (3) a field applied to chemical cross-linking of the matrix polymer chains. The fields (1) and (2) initially develop fluctuations in a spatial dispersion of filler particles in polymer matrices. The fluctuations are subsequently grown into the self-organized dissipative structures of the filler particles in the polymer matrices, which are eventually locked or arrested at nonequilibrium in the cross-linked network chains of the polymers by the field (3). We investigate the locked, static dissipative structures to gain insight into the self-organization process. As model filler/polymer nanocomposites, we focus on carbon black filler particles dispersed in poly(styrene-*ran*-butadiene) (SBR) and carbon black filler particles dispersed in polyisoprene (PI), which are designated as CB/SBR and CB/PI, respectively.

Rubber/filler composites, which comprise one of the most successful composites and exhibit the viscoelastic properties of soft rubbers as well as hard mechanical characteristics and some functional characteristics of filler particles [3–5], have been improved to satisfy increasing demands on their performance, e.g., performance for their application to economic and ecological car tires. From these technological points of view, the dissipative structures of the NPs in the polymer matrices should be controlled at will by manipulating effective interactions between the filler particles and the polymers in given compounding (mixing) conditions. A chemical modification of the polymer is anticipated to effectively promote its affinity for the fillers. The composites that consist of the SBR modified by the amino- and alkoxysilyl-groups at one of the chain ends altered the self-organized dissipative structures of CB and silica filler particles [6] and exhibited a considerable improvement in the mechanical properties with respect to the loss tangent (tan δ) and the nonlinear Payne effect [7]. The manipulations also include the addition of additives, such as coupling reagents or accelerators, in the systems to enhance the chemical affinity of the polymers for the fillers [8].

The self-organized dissipative structures of the filler particles locked at nonequilibrium by cross-linking the matrix polymers (SBR and PI) were investigated over a wide length scale that ranged from ~0.1 nm to ~20 μm using combined wide-angle X-ray scattering (WAXS), small-angle X-ray scattering (SAXS), ultra-SAXS (USAXS), small-angle neutron scattering (SANS), and ultra-SANS (USANS). The combined scattering methods (CSAS) enabled us to systematically explore statistically averaged information over a large sample area concerning the dissipative structure of the filler particles in three-dimensional (3D) space.

II. Experimental methods

The experimental methods relevant to this article are summarized as follows:

II-1. Sample characterizations

A CB filler (SHOBLOCK N339, Showa Cabot, Chiba, Japan) was employed in this study. The mean radius of the primary particle of the CB filler as determined by transmission electron microscopy (TEM) ($R_{\mathrm{P,TEM}}$) was 13 nm. The density of the CB filler was 1.82 g/cm^3. The rubbery polymers in this study were PI (ZEON Co., Kawasaki, Japan) and SBR (ZEON Co.); their characteristics are listed in Table 1. The volume fraction of the CB filler was fixed to 20%, the high loading of which is typically required in commercial applications for enhancing the mechanical properties of rubbers. The specific surface areas measured using the nitrogen adsorption method and the dibuthyl phthalate absorption for the CB filler were determined to be 90 m^2/g and 1.18 ml/g, respectively. Characterizations of the CB-filled rubber compounds are listed in Table 2. The CB filler was compounded into the polymers using a Banbury mixer at 60 rpm for 5 min with the chamber temperature heated to $T = 80$ °C for the first-step mixing to prepare a master batch. The master batch of CB/polymers were mixed with di-*t*-butyl peroxy diisopropyl benzene as a cross-linking agent using an open roll mill at ~20 rpm and $T = 40$–60 °C for the second-step mixing, as shown in Table 3. The uncrosslinked sheets and cross-linked sheets of the CB/polymers compounds were subsequently prepared by pressing the compounds in a mold at $T = 100$ °C for 4 min and at 170 °C for 20 min, respectively. The dissipative structures, which are self-organized during the first-step mixing, second-step mixing, and subsequent molding process into the sheets, can be arrested at nonequilibrium at the time when the polymers are crosslinked.

II-2. USANS measurements

The USANS measurements were conducted with the PNO spectrometer installed at the beam line of the JRR-3 research reactor at JAEA in Tokai, Japan. Details of the USANS setup have been described elsewhere [9]. Two single-bounce silicon (111) single crystals were employed; the first crystal is employed to monochromatize and collimate the incident beam, and the second crystal is to analyze the scattered beam. The scattering intensity from the CB filler excess to the background scattering from the empty cell was observed in the entire q-range between $q_{\min} \approx 3.0 \times 10^{-4}\,\mathrm{nm}^{-1}$ and $q_{\max} \approx 1 \times 10^{-2}\,\mathrm{nm}^{-1}$, where $q \equiv (4\pi/\lambda)\sin(\theta/2)$ is the

Table 1 Characterizations of polymers used in this study

Polymers	M_w	M_w/M_n	w_{PS} (%)[a]	Vinyl content (%)[b]	T_g (K)[c]
SBR	5.0×10^5	3.4	23.5	15	219
PI	1.2×10^6	2.7	–	–	208

[a] Weight fraction of styrene content in SBR

[b] Vinyl content in butadiene sequence in SBR

[c] The glass transition temperature measured by the DSC with the heating rate of 10 °C/min

Table 2 CB-filled rubber compounds used in this study

Code name	Polymers	ϕ_{CB}[a]	w_{cr} (wt%)[b]	w_{PO} (wt%)[c]
CB/SBR (20)	SBR	20	0.8	15
CB/PI (20)	PI	20	1.4	–
CB/PI (20)/UCR[d]	PI	20	–	–

[a] Volume fraction of filler particles

[b] Weight fraction of peroxide crosslinker

[c] Weight fraction of process oil

[d] UCR designates uncross-linked PI matrix

Table 3 Compounding processes and conditions of CB/polymers[a]

Compounding processes Conditions	First-step process (Banbury mixer)	Second-step process (Roll mill)
Mixing rate (rpm)	60	~20
Chamber temperature	80 °C	40–60 °C
Period	5 min	–
Bulk components	CB powder and SBR, PI	Cross-linker and master batch[b]

[a] The compounds prepared after the first-step process and second-step process were molded into sheets at 100 °C for 4 min to prepare un-crosslinked sheets and 170 °C for 20 min to prepare cross-linked sheets

[b] The compounds prepared by the first step process

magnitude of the scattering vector, and λ and θ are the wavelength of the incident beam and the scattering angle, respectively. Thus, this q-range was utilized for this study.

II-3. USAXS measurements

The USAXS based on the synchrotron radiation were performed at the beam line BL03XU of the SPring 8 at the Japan Synchrotron Radiation Research Institute (Hyogo, Japan). The lab-based USAXS camera has also been employed; details are provided elsewhere [10]. Four-bounced (220) Bragg reflections from germanium channel-cut crystals (Bragg angle is 22.65° with CuKα_1 radiation) were utilized in both the monochromator and the analyzer. Due to a newly installed asymmetric Bragg reflection mixed in the conventional rigid monochromator, the incident beam flux can be increased by a factor of four compared with that without the installation [10, 11]. With our USAXS apparatus, the scattering profile in the q-range of 0.002–0.45 nm^{-1} can be measured. This q-range partially overlapps with those in which the USANS and SAXS profiles are measured, Thus, the use of USAXS overcomes the demerit caused by the high-intensity background in the large q tail of the USANS and caused by the low q resolution limit of SAXS.

II-4. SAXS measurements

The SAXS based on the synchrotron radiation were performed at the beam line BL03XU of the SPring-8 at the Japan Synchrotron Radiation Research Institute (Hyogo, Japan). SAXS profiles were also taken with a lab-based apparatus that consists of an 18 kW rotating-anode X-ray generator with a cooper target (M18XHF-SRA, MAC Science Co., Ltd. Yokohama, Japan, now Bruker AXS K.K. Yokohama, Japan), a graphite monochromator, a 2.0 M camera from the sample to the detector and a one-dimensional position sensitive proportional counter. An exposure time for each measurement was set to 30 min for the experiments with the in-house SAXS apparatus. The contribution of thermal diffuse scattering (TDS) to the measured scattering profiles in the higher q-region should be corrected. TDS is known to be caused by acoustic phonons that propagate in the scattering media. The scattering intensity of the TDS—$I_{TDS}(q)$—in the q-range in this experiment is approximated by [12]

$$I_{TDS}(q) = I_{TDS}(0)\exp\left(cq^2\right), \tag{1}$$

where c is a constant independent of q, and $I_{TDS}(0)$ is an extrapolated scattering intensity at $q = 0$. The $I_{TDS}(0)$ values were estimated from the best-fit between Eq. (1) and the experimental data in the q-region at $28 < q^2 < 43$ nm^{-2}, where the ln$I$ (q) vs. q^2 plots show a linear relationship [2].

The film thickness of each sample was optimized for the X-ray scattering measurements, i.e., $\mu t = 1$, where μ is the linear absorption coefficient of X-ray for the system to be analyzed and t is the film thickness. All samples were measured at room temperature at atmospheric pressure. The USANS, USAXS, and SAXS scattering profiles were corrected for the air scattering, absorption, and slit-width and slit-height smearing. X-ray scattering data were measured on an absolute intensity scale using the nickel-foil method [13], and the neutron scattering profiles were vertically shifted to match the X-ray scattering profiles with an overlap q-range on the logarithmic intensity scale. The vertical shift of the neutron scattering data in the logarithmic scale corresponds to a conversion of the absolute scattering intensity scale of the neutron scattering profiles to that of the X-ray scattering intensity for a given system (CB/polymer composites) of our interest, the basic principles of which have been presented elsewhere [14]. Therefore, we specify the absolute intensity scale of the combined X-ray and neutron scattering intensity profiles shown in Figs. 5 and 6 with respect to that of the X-ray.

II-5. TEM experiments

The CB/SBR(20) and CB/PI(20) composites were microtomed at $T = -100\,°C$, using a LEICA Ultracut UCT sectioning system (LEICA Microsystems K.K., Tokyo, Japan). The ultrathin sections with a thickness ~100 nm without staining were employed for observations under a transmission electron microscope at 200 kV (H-800, Hitachi, Tokyo, Japan).

III. Results

III-1. Characterization of powder of CB filler particles

A bulk of the CB filler powder is mixed with a bulk of rubbery polymers and then molded into sheets of the CB/polymer composites. The compounding process involves a transformation of the initial structures of CB filler particles in the pure powder that are dispersed in air through interparticle attractive interaction into the final structures of CB filler particles dispersed in the polymer matrices. Thus, investigating the initial filler particle structures in the CB powder in air is crucial to gain insight into the transformation process and the self-organization mechanism of the filler particles in the polymer matrices. The CB powder, viz., the CB filler particles dispersed in air, is designated as CB/Air.

Figure 1 shows the combined USAXS and SAXS profiles from CB/Air [$I_{\mathrm{exp}}(q)$ presented by unfilled circles], which were measured by the synchrotron X-ray incident beam source and corrected for the TDS. The broken and solid profiles [$I_{\mathrm{theor}}(q)$] will be discussed in Section IV. For the scattering experiments, the pelletized CB powder used for mixing with the polymers was packed in a sample cell. The volume fraction of the CB particles in the filler powder in the cell $\phi_{\mathrm{CB,air}}$ was estimated to be 0.06 from the ratio of the measured density of the filler in the cell and the reported density for the CB filler. The experimental result presented in Fig. 1 will be concurrently discussed later with that in Fig. 2 because the two systems are expected to have similar scattering behaviors.

The pelletized powder was further grinded into finer powder with a pestle and mortar to a level where the original appearances of the pelletized powder could not be distinguished. The grinded finer powder was further dispersed in toluene to weaken the physical bonding between the particles due to the interparticle attractive force. We further applied sonic energy to the dispersion of the CB filler particles in toluene using an ultrasonic cleaner for 60 min. The particles were completely precipitated to prepare the sample designated as CB/Toluene (20), which contains particles with a volume fraction of 0.2 in the medium of toluene. Figure 2 shows the combined USAXS and SAXS profiles $I_{\mathrm{exp}}(q)$ from CB/Toluene (20) presented by unfilled circles. The broken and solid profiles $I_{\mathrm{theor}}(q)$ indicate a theoretical analysis of the experimental profile that will be discussed in Section IV.

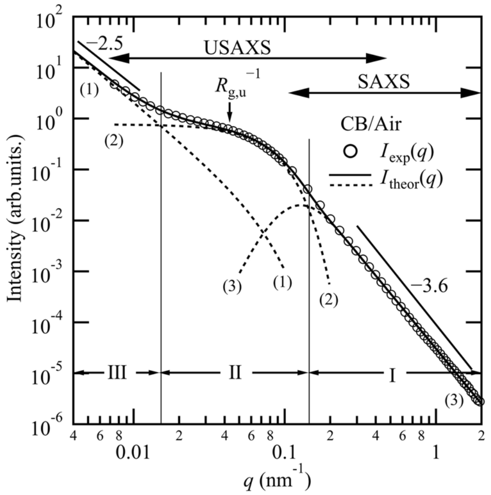

Fig. 1 Combined USAXS and SAXS profiles for CB powder (CB/Air, $I_{\mathrm{exp}}(q)$, unfilled circles). The broken lines numbered (1)–(3) contribute to the first term to third term in the rhs of Eq. (5) to the net theoretical scattering profile shown by the solid line drawn through the unfilled circles

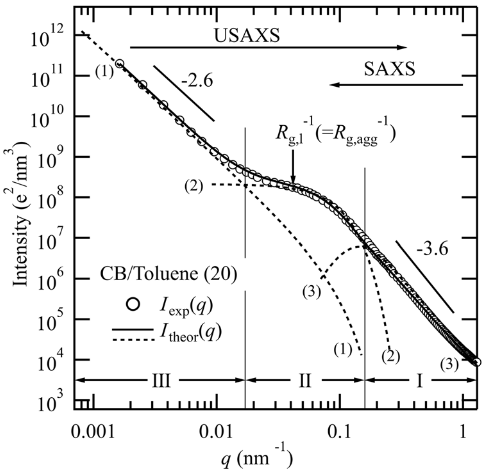

Fig. 2 Combined USAXS and SAXS profiles for CB/Toluene(20) [$I_{\mathrm{exp}}(q)$, unfilled circles]. The solid and broken lines numbered 1–3 have the same meaning as in Fig. 1

The scattering profile $I_{\mathrm{exp}}(q)$ in the high q-region ($q > 0.14\,\mathrm{nm}^{-1}$) designated as Region I and that in the low q-region ($q \lesssim 0.015\,\mathrm{nm}^{-1}$) designated as Region III depends on q according to a power law,

$$I_{\mathrm{exp}}(q) \sim q^{-p}, \tag{2}$$

where $p = 3.6$ and 2.5 in Region I and Region III, respectively, in Fig. 1 and $p = 3.6$ and 2.6 in Region I and Region III, respectively, in Fig. 2.

The power-law dependence $I_{\mathrm{exp}}(q)$ in the high q-region (Region I) was attained with high accuracy by the combined SAXS and WAXS, as shown in Fig. 3 for CB/Toluene (20). In Fig. 3a, the WAXS data were vertically shifted in the logarithmic intensity scale to match the SAXS profile with a sufficiently wide overlap q-region, as shown in the figure. In the WAXS profile, we observe the two peaks indicated by two arrows: a broad amorphous peak at $q_a = 15.4\,\mathrm{nm}^{-1}$ and a relatively sharp peak at $q_c = 17.7\,\mathrm{nm}^{-1}$, which is attributed to (002) diffraction with a Bragg spacing ($d_{002} = 2\pi/q_{\mathrm{c}}) = 3.56$ Å. The values q_{a} and q_{c} at these peaks were determined by the best-fit of the experimental WAXS profile with the predicted profile constructed by a weighted average of Lorentzian and Gaussian functions for the broad components and sharp components, respectively. Each contribution is shown by the broken line marked as (1) and the broken line marked as (2), respectively. Note that the d_{002} value determined by WAXS is slightly larger than that for an ideal graphite crystal ($d_{002} = 3.35$ Å), which is commonly encountered in CB with internal inhomogeneous (i.e., turbostratic) structures [15].

To extract the SAXS profile in Region I with high accuracy, we subtracted the contribution of the broad Lorentzian component [profile (1)] from the net combined SAXS and WAXS profile (shown by the unfilled circles). The corrected SAXS profile obtained by the subtraction is shown by the profile marked by (3) in Fig. 3a. Figure 3b shows the corresponding SAXS profile in the q-range from 0.3 to $5\,\mathrm{nm}^{-1}$ [unfilled symbols labeled by (3) with the expanding q scale]. The power law with $p = 3.6$ shown by the broken line is observed at $0.3 < q < 1\,\mathrm{nm}^{-1}$ in Figs. 2 and 3b, the exponent of which shows agreement with the previous SANS experiments that yielded $p = 3.67$ regardless of whether the CB grades differed [16]. However, at the higher q-range of $q > 1\,\mathrm{nm}^{-1}$, we observe a deviation from the power-law scattering as shown in Fig. 3b. We postulate that this excess scattering is attributed to internal inhomogeneities (turbostratic structure) in the CB particles, which comprise crystalline and amorphous phases, as will be shown in part (a-1) of Fig. 8a.

The scattering profiles shown in Figs. 1 and 2 commonly indicate the power-law profiles in Region I and III. The scattering profile in Region I in Fig. 1 is identical to that in Fig. 2, viz., they are independent of the dispersion media. The power-law profile in Region III in Fig. 1 differs from that in Fig. 2, viz., they depend on the dispersion media. These results indicate that the smallest structural unit illuminated by the profile in Region I must reflect the filler particles, whereas the large structure unit illuminated by the profile in Region III must reflect agglomerates of the filler particles, because the dispersion medium (air or toluene) affects the agglomerates through the medium-dependent interparticle attractive interaction.

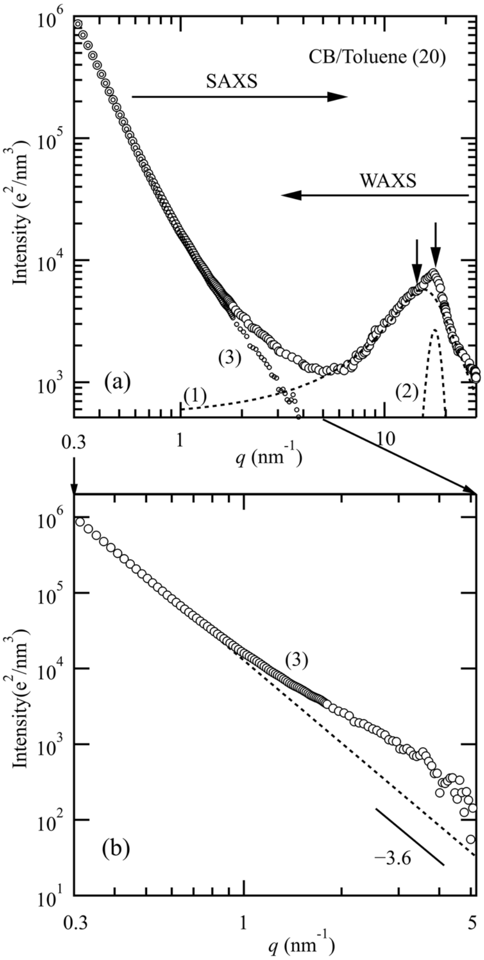

Fig. 3 **a** Combined SAXS and WAXS profiles for CB/Toluene(20) (unfilled circles). The arrows indicate the peak positions for the broad and sharp profiles that contribute to the net WAXS profile. The broken line (1) and broken line (2) show the broad peak approximated by a Lorentzian function and the sharp peak approximated by a Gaussian function, respectively. The profile (3) is the SAXS profile after the subtraction of the broad profile (1) in WAXS, **b** Corrected SAXS profile (3) $I_{\mathrm{corr}}(q)$ (symbols) obtained after subtracting the profile (1) from the combined SAXS and WAXS profiles by the correction method described in part (**a**)

The power-law exponent $p_1 = 3.6$ in Region I that satisfies $3 \le p_1 \le 4$ suggests that the smallest structural unit of the filler particles has the surface fractal [17, 18] with its fractal dimension $D_s = 2.4$, because p_1 is related to D_s by

$$p_1 = 2d - D_s, \quad 3 \leq D_s \leq 4, \tag{3}$$

where d is the Euclidean dimension of the space (in this case, $d = 3$). The power-law exponent $p_2 \cong 2.5$ in Region III in Fig. 1 and the power-law exponent $p_2 = 2.6$ in Region III in Fig. 2 satisfy $1 \leq p_2 \leq 3$, which suggests that the agglomerate has the mass fractal with its fractal dimension $D_m = 2.5$ in Fig. 1 and $D_m = 2.6$ in Fig. 2 because p_3 is related to D_m by

$$p_2 \equiv D_m. \tag{4}$$

The discussion regarding the scattering profiles in Regions I and III reasonably leads us to conclude that the scattering profile in Region II must reflect the lower cut-off structures that build up the mass-fractal agglomerates (defined as **MFAs**) in the given dispersion medium. We define the lower cut-off structure of the MFAs as "**cluster**", the detail structure of which will be clarified in Section IV-2.

III-2. Characterization of CB/SBR(20) and CB/PI(20) after cross-linking

III-2.1. Characterization with TEM

Figure 4 shows representative TEM images for CB/SBR (20) at low magnification and high magnification (part a and part b, respectively) and those for CB/PI(20) at low magnification and high magnification (part c and part d, respectively). The CB particles appeared to be dark, whereas the SBR and PI matrices appeared to be bright. In the high magnification TEM images shown in parts (b) and (d), we can identify the primary particles with a diameter of ~26 nm and the aggregates with a diameter of ~54 nm as represented by the yellow circles labeled as P and the red circles labeled as A, respectively. We note that the primary particles were hardly isolated; the primary particles were assembled closely together or were more likely fused to form the aggregates.

The primary particles (P) and the aggregates (A) for CB/SBR(20) and CB/PI(20) are identical because the same CB was employed. However, the TEM images may imply a difference in how the aggregates are linked to form the building blocks, which further build up agglomerates, viz., a higher-order structure of the filler particles. The TEM images in parts (b) and (d) tend to imply that the building block consists of two linearly interconnected aggregates and three linearly interconnected aggregates, respectively, of A, viz., AA sequence and AAA sequence, respectively. The building blocks appeared to be further interconnected in 3D space, as shown locally in parts (b) and (d), to form higher-order structures of the MFAs, as shown globally in parts (a) and (c), which is common for both CB/SBR(20) and CB/PI(20).

Although the MFAs for both CB/SBR(20) and CB/PI (20) may commonly have a structure characterized by self-similarly branched dendrites, the branches in the two samples appear to differ, which reflects the difference in the building blocks: the branches for CB/PI(20) appear to have a larger anisotropy in their shapes than those for CB/SBR (20). However, the quantitative characterizations of the MFAs from the TEM images may experience some difficulty because the space covered by TEM is limited, especially along the thickness direction of the ultrathin sections. Moreover, structural elements that exist along the thickness direction, are overlapped in the TEM images. Although the TEM images may visualize the existence of the MFAs, quantitatively characterizing basic information about the MFAs, such as their lower and upper cut-off sizes, the lower cut-off structural entity (building block), and the fractal dimension may be difficult. These basic piecies information, which are statistically averaged over a large sample area, are quantitatively obtained by the CSAS method.

III-2.2. Characterization with CSAS

Figure 5 presents the experimental scattering profile $I_{exp}(q)$ shown by the unfilled circles for the peroxide cross-linked CB/SBR(20) obtained by a combined use of USANS, USAXS, and SAXS, which encompasses the scattered intensity over the wide q-range of 3.0×10^{-4}–$1.5\ \mathrm{nm}^{-1}$ (corresponding length scale r is approximately 4 orders of magnitude, ranging from a few nm to a few 10 μm, as shown in the top abscissa). The intensity scale is also wide —approximately 10 orders of magnitude. The solid line in part (a) and the broken lines in part (b) present the theoretical profiles $I_{theor}(q)$ to be discussed in Section IV. We observe three power-law scattering profiles given by Eq. (2). At the high q-range ($0.2 < q < 1.5\ \mathrm{nm}^{-1}$) inside Region I, the power-law behavior with $p_1 = 3.40 \pm 0.04$ is observed, which suggests that the surface of the smallest structural unit of the particles is not smooth but is self-similarly rough characterized by $D_s = 2.6$ (refer to Eq. (3)), as will be clarified in Section IV-1. According to the previous SANS experiments [16], the pure CB filler at the high q-region was determined to be $p_1 = 3.67$, regardless of the CB grades. This power-law exponent is substantially larger than that of CB/SBR(20), but shows agreement with our SAXS data for CB/Air and CB/Toluene ($p_1 = 3.6$), as shown in Figs. 1 and 2. The physical significance of the disparity in p_1 between CB/SBR(20) and the CB powder in air and toluene is discussed in Section IV-4.

The power-law exponent with $p_2 = 2.45 \pm 0.03$ is observed in the q-range from ~0.002 to ~0.015 nm^{-1} [defined as Region III in Fig. 5], which indicates that

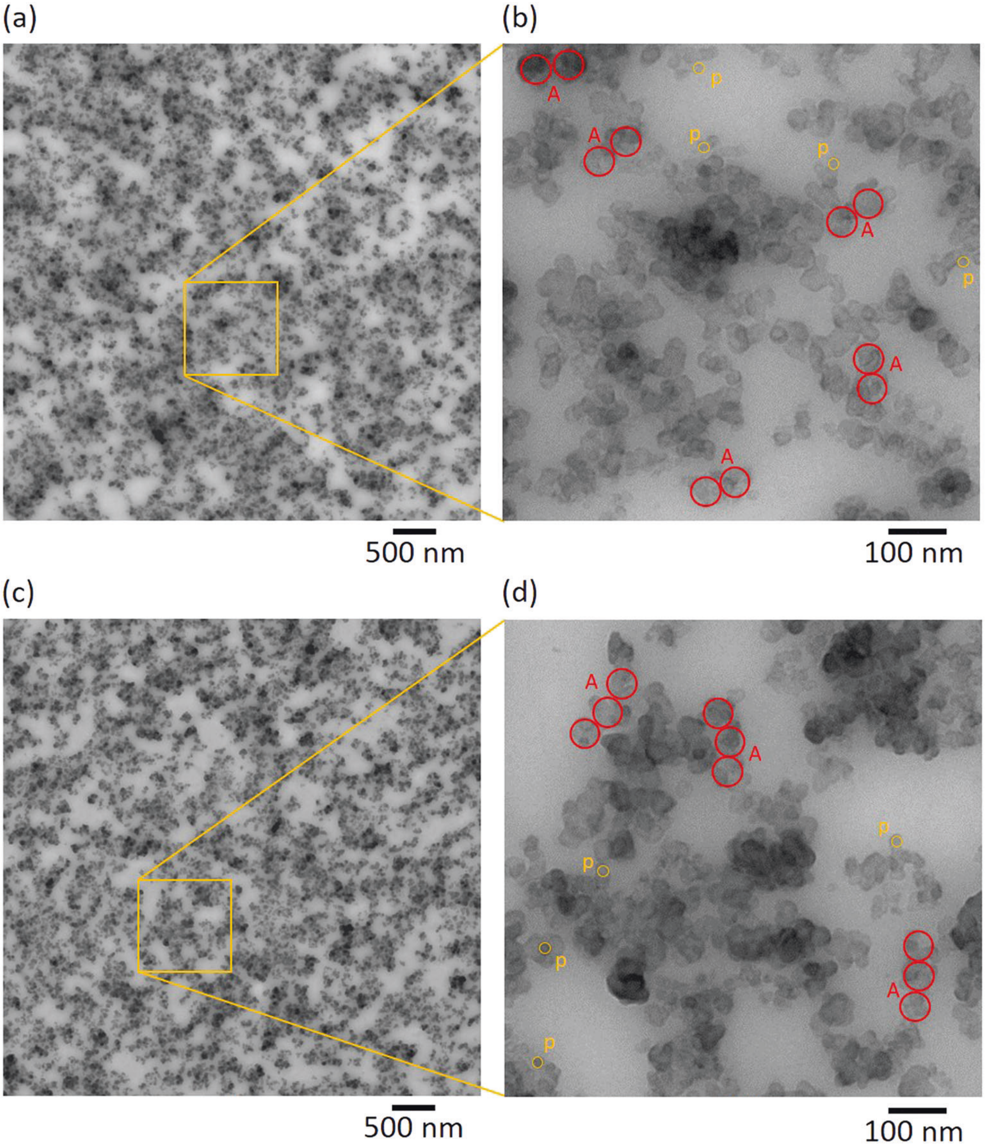

Fig. 4 TEM for CB/SBR(20) with a low magnification (part **a**) and a high magnification (part **b**) and TEM for CB/PI(20) with a low magnification (part **c**) and a high magnification (part **d**). The circles labeled by P and A represent primary particles and aggregates, respectively

existence of MFA with a mass fractal dimension $D_m = 2.45$ given by Eq. (4). The apparent power law with $p_3 \cong 3.7$ is observed at the very low q-range of $\sim 0.0003 < q < \sim 0.0006\,\mathrm{nm}^{-1}$, as defined in Region V in Fig. 5. The term “apparent” is coined because the power law is only observed over the very narrow q-range due to a limitation of the low q-resolution of the USANS apparatus for this particular sample. The scattering in this q-range depends on a higher-order superstructure that is built up by MFAs, viz., the hierarchy level structure (level 5) higher than that of MFAs (level 4), to be discussed in Section IV-2 in conjunction with Fig. 8. The power law exponent $p_3 \cong 3.7$ may indicate that surfaces of the MFAs, which are packed in space, may form the fractal structure with the surface fractal dimension $D_s = 6 - p_3 \cong 2.3$.

Another important aspect in the scattering profile for CB/SBR(20) is the two discrete form-factor profiles, which can be assumed by Gaussian functions (Guinier scattering functions), as indicated by the arrows in Fig. 5a, b. The positions of the arrows correspond to ${R_{g,u}}^{-1}$ and ${R_{g,l}}^{-1}$, where $R_{g,u}$ and $R_{g,l}$, respectively, correspond to the upper cut-off length and lower cut-off length, respectively, of the mass fractal structure with $D_m = 2.45$, as will be clarified in Section IV-1.

Note that (i) the power law of $q^{-3.4}$ is observed to persist at $q \gtrsim q_s = 0.2\,\mathrm{nm}^{-1}$, which implies that the lower

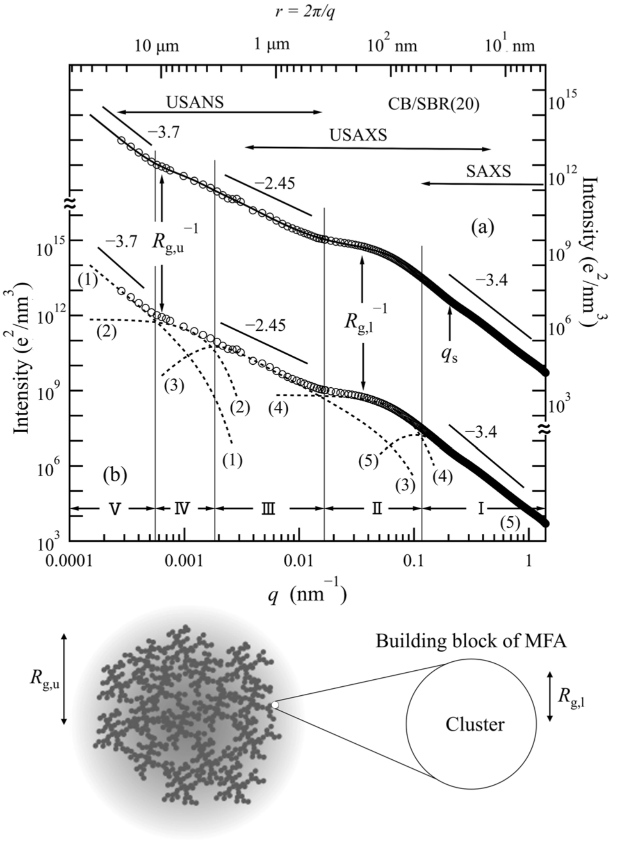

(c) Mass-fractal Agglomerate (MFA)

Fig. 5 **a** Combined USANS, USAXS, and SAXS profiles for CB/SBR (20) $I_{\mathrm{exp}}(q)$ (unfilled circles), where the USANS intensity is converted to the absolute intensity scale of X-ray scattering (the intensity scale should be referred to the rhs ordinate). The two arrows denoted by $R_{\mathrm{g,u}}{}^{-1}$ and $R_{\mathrm{g,l}}{}^{-1}$ infer the existence of Guinier scattering functions with radii of gyrations $R_{\mathrm{g,u}}$ and $R_{\mathrm{g,l}}$, which suggest the upper cut-off length and lower cut-off length, respectively, for the mass-fractal agglomerates with $D_{\mathrm{m}} = 2.45$. The solid line is the best-fitted scattering function $I_{\mathrm{theor}}(q)$ based on Eq. (6). **b** The broken lines numbered (1) to (5) represent the contribution of the first term to the fifth term in the rhs of Eq. (6) to the net $I_{\mathrm{theor}}(q)$ (intensity scale should be referred to the left-hand side ordinate). **c** Schematic of the mass-fractal agglomerate (MFA) with the upper cut-off length $R_{\mathrm{g,u}}$ (left) and the lower cut-off length $R_{\mathrm{g,l}}$ (right). $R_{\mathrm{g,l}}$ is the radius of gyration of the cluster as a building block of the MFA

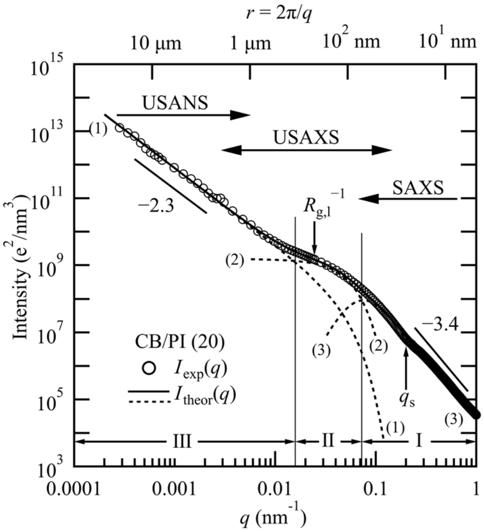

Fig. 6 Combined USANS, USAXS, and SAXS profiles for CB/PI(20) [$I_{\mathrm{exp}}(q)$, symbols]. The solid line denotes the best-fitted theoretical profile $I_{\mathrm{theor}}(q)$ obtained from Eq. (5). The broken lines numbered (1) to (3) denote the contribution of the first term to the third term in rhs of Eq. (5) to $I_{\mathrm{theor}}(q)$

cut-off wave number q_{s} for the surface fractal object is approximately 0.2 nm^{-1} (as will be clarified in Section IV-1.2. in conjunction with Fig. 5b), and (ii) this value q_{s} is substantially larger than the upper cut-off wave number $R_{\mathrm{g,l}}{}^{-1} \cong 0.034$ nm^{-1} of the MFAs. Facts (i) and (ii) reveal that the self-similar surface roughness exists on the surface of the aggregates and the primary particles that comprise the lower cut-off object (i.e., cluster) with the characteristic length $R_{\mathrm{g,l}}$. This fact causes a crossover in the q-dependence of $I_{\mathrm{exp}}(q)$ around $q \cong q_{\mathrm{s}} = 0.2$ nm^{-1}: the q-dependence at $R_{\mathrm{g,l}}{}^{-1} < q < q_{\mathrm{s}}$ depends on that of the structure factor of the cluster which yields a broad scattering profile with q, whereas $q > q_{\mathrm{s}}$ is controlled by the surface roughness of the aggregates, which yields q^{-p_1} [$p_1 = 3.4$ for CB/SBR(20)], as experimentally obtained. However this crossover, in the q-dependence of $I_{\mathrm{exp}}(q)$ in Region I, does not imply existence of a shoulder at $q = q_{\mathrm{s}}$ due to the form-factor peak from either the primary particle or the aggregate: the q value for the form-factor peak q_{P} should appear at $q_{\mathrm{P}} = 0.44$ nm^{-1} based on $U_{\mathrm{max}} \equiv q_{\mathrm{P}} R_{\mathrm{s,P}}$ with $U_{\mathrm{max}} \equiv 5.76$ [19] and the known value of $R_{\mathrm{s,P}} = 13$ nm, which is the average radius of the primary particle. The aggregates have a broad size distribution so that it would not yield the form factor peak or shoulder. This trend is valid for all samples in this study. The CB powder in this work is believed to exhibit no form-factor peaks or shoulders due to a large polydispersity of $R_{\mathrm{s,P}}$ and $R_{\mathrm{s,agg}}$.

Figure 6 shows the combined USANS, USAXS, and SAXS profiles for the peroxide cross-linked CB/PI(20) [$I_{\mathrm{exp}}(q)$, unfilled circles]. The profile presented by the solid line and the broken lines numbered (1)–(3) are theoretical profiles $I_{\mathrm{theor}}(q)$ to be discussed in Section IV-1. In the figure, we observe the two power-law scattering profiles in Region I and III and the Guinier scattering in between them. However, no upper cut-off length is detected for the power-law scattering in Region III in the covered small q-range, which indicates that the size of the upper cut-off length for the mass-fractal structure is larger than the USANS resolution limit of 21 μm ($=2\pi/q_{\mathrm{min}}$) and considerably larger than that for CB/SBR(20). As will be discussed later, the lower cut-off length ($R_{\mathrm{g,l}}$) is also considerably larger than that for CB/SBR(20) shown in Fig. 5, whereas the power-law exponents in Region III (2.3) for CB/PI(20) is smaller than that for CB/SBR(20) (2.45). This finding indicates that the mass-fractal dimension D_m (=2.3) for CB/PI(20) is smaller than that (=2.45) for CB/SBR(20), although the surface fractal dimensions remained unchanged with the change in the rubber matrix, as revealed by the same power-law exponent p_1 (=3.4).

IV. Analyses of scattering profiles and discussion

IV-1. Analyses based on the unified Guinier law/ Power law approach

IV-1.1. CB/Air, CB/Toluene(20), and CB/PI(20) after cross-linking

The scattering profiles for the pure CB powder in air and the pure CB powder in toluene (CB/Air and CB/Toluene (20), respectively) and CB/PI(20) after the cross-linking of PI as presented in Figs. 1, 2, and 6, respectively, are commonly composed of the two power-law profiles, which reflect the surface fractal structural unit in Region I and the MFAs of the filler particles in Region III, and the profile related to the lower cut-off object of the MFAs in Region II. These characteristic scattering profiles can be described by the theoretical scattering function defined by $I_{\text{theor}}(q)$, which is based on the unified Guinier-law/power-law approach proposed by Beaucage [20] (defined by UFGPA),

$$\begin{aligned} I_{\text{theor}}(q) \;&=\; C\exp\left(-q^2R_{g,l}^2/3\right)q^{-p_2} \\ &+D\exp\left(-q^2R_{g,l}^2/3\right)+E\left[\operatorname{erf}\left(qR_{g,l}/\sqrt{6}\right)\right]^{3p_1}q^{-p_1} \end{aligned} \tag{5}$$

where C, D, and E are the proportionality constants that control a relative contribution of each term to the net $I_{\text{theor}}(q)$. The scattering function given by the Guinier law $\exp(-q^2R^2_{g,l}/3)$ contributes to $I_{\text{theor}}(q)$ by the first and second terms on the right-hand side (rhs) of Eq. (5) as follows: (i) it damps the power-law profile of q^{-p_2}, $p_2 = D_m$ in the q-region larger than that in Region III, i.e., in Regions II and I, as given by the contribution of the profile (1) presented by the broken line to the net $I_{\text{theor}}(q)$ drawn by the solid line through the experimental profile shown by the unfilled circles and (ii) it contributes to the net $I_{\text{theor}}(q)$, as given by profile (2) presented by the broken line. The term related to the Gauss' error function in the third term of the rhs in Eq. (5) contributes to damping the power law profile of q^{-p_1}, $p_1 = 2d - D_s$, in the q-region smaller than that of Region I, i.e., in Region II, as given by profile (3), which is also presented by a broken line. The characteristic parameters analyzed by best fitting between $I_{\exp}(q)$ and $I_{\text{theor}}(q)$ are summarized in part of Table 4.

Table 4 Characteristic parameters estimated by the best fitting of the experimental scattering profiles $I_{\exp}(q)$ with $I_{\text{theor}}(q)$ based on UFGPA

Parameters Samples (K)	$(R_{g,u})_K$[a] μm	$(R_{g,l})_K$[b] nm	$(D_m)_K$	$(D_s)_K$
CB/Toluene (20)	Undetermined[c]	21[f] (27[g])	2.6	2.4
CB/Air	Undetermined[d]	24 (31[g])	2.5	2.4
CB/SBR (20)	1.6	29 (37[g])	2.45	2.6
CB/PI (20)	Undetermined[e]	40 (52[g])	2.3	2.6

[a] The radius of gyration of the upper cut-off of the mass-fractal agglomerates.

[b] The radius of gyration of the lower cut-off structure (cluster), which builds up the mass-fractal agglomerates of the filler particles.

[c–e] $R_{g,u}$ was unable to be determined because $R_{g,u}{}^{-1} < q_{\min}$, which is the minimum value of q accessed by the experiments. $R_{g,u}$ is expected to be larger than $q_{\min}{}^{-1}$ nm, i.e., 714 nm, 143 nm, and 2.1 μm at least in the case of c, d, and e, respectively.

[f] The lower cut-off structure defined as "cluster" is identical to the aggregate in the case of CB/Toluene (20).

[g] The average radius of sphere that corresponds to $R_{g,l}$.

IV-1.2. CB/SBR(20) after cross-linking

The experimental scattering profile $I_{\exp}(q)$ shown by the unfilled circles in Fig. 5 was best-fitted with the theoretical profile $I_{\text{theor}}(q)$ based on UFGPA given by

$$\begin{aligned} I_{\text{theor}}(q) = A\,&\exp(-q^2R_{g,u}^2/3)q^{-p_3} + B\exp(-q^2R_{g,u}^2/3) \\ &+C\exp(-q^2R_{g,l}^2/3)\left[\operatorname{erf}(qR_{g,u}/\sqrt{6})\right]^{3p_2}q^{-p_2} \\ &+D\exp(-q^2R_{g,l}^2/3)+E\left[\operatorname{erf}(qR_{g,l}/\sqrt{6})\right]^{3p_1}q^{-p_1} \end{aligned} \tag{6}$$

Based on this equation, the net scattering profile was decomposed into the five elemental profiles, as shown by the broken lines numbered (1)–(5) in Fig. 5b. Each profile has the following characteristics: Profile (1), which is given by the first term in the rhs of Eq (6), is composed of the term that represents the power-law scattering q^{-p_3} with $p_3 = 3.7$ and the term that represents the Guinier scattering function with the radius gyration $R_{g,u}$, which corresponds to the lower cut-off length for this power law. The latter term serves as a damping factor for this power law at $q > R_{g,u}{}^{-1}$. Profile (2) given by the second term in the rhs of Eq (6) represents the Guinier scattering function with the radius of gyration $R_{g,u}$ which corresponds to the upper cut-off length of the MFAs with $p_2 = D_m = 2.45$ as well, as shown by the arrow labeled by $R_{g,u}$ in the left half of Fig. 5c. Profile (3), which is given by the third term in the rhs of Eq (6) with $p_2 = D_m = 2.45$, represents the power-law scattering profile $I(q) \propto q^{-D_m}$ with the upper cut-off length of $R_{g,u}$ and the lower cut-off length of $R_{g,l}$ which is shown by the arrow labeled by $R_{g,l}$ in the right half of Fig. 5c. The term $\left[\mathrm{erf}\left(qR_{g,u}/\sqrt{6}\right)\right]^{3p_2}$ serves as a damping factor for the power law in the small q-range in Regions IV and V, whereas the term $\exp(-q^2R^2_{g,l}/3)$ serves as a damping factor for the power law in the large q-range in Regions II and I. Profile (4), which is given by the fourth term in the rhs of Eq (6), represents the Guinier scattering function with a radius of gyration of $R_{g,l}$ for the lower cut-off structure, viz., the cluster which builds up the MFAs with $p_2 = D_m = 2.45$. Profile (5), which is given by the fifth term of the rhs of Eq (6) with $p_1 = 2d{-}D_s = 3.4$, represents the power-law scattering profile of $I(q) \propto q^{-p_1}$ with the upper cut-off length $R_{g,l}$. The term $\left[\mathrm{erf}\left(qR_{g,1}/\sqrt{6}\right]^{3p_1}\right.$ serves as a damping factor for the power-law in the small q-range in Region II.

Note the following points: the power law of $q^{-3.4}$ is observed at $q \geq q_s = 0.2\,\mathrm{nm}^{-1}$, where q_s is greater than $R_{g,l}^{-1}$. Thus, the self-similar surface roughness should exist on the surface of the aggregates and primary particles, which reconfirms the argument that is previously given in Section III-2.2. The power law of $q^{-3.7}$ observed in Region V reflects in principle the fact that this hierarchical structure level is higher than that of the MFAs: the surfaces of the MFAs packed in space further form surface fractal structures with $D_s = 6{-}p_3 \cong 2.3$.

The solid line in Fig. 5a shows the sum of the scattering profiles (1)–(5) shown in Fig. 5b. We confirm that the sum of each scattering profile gives the best-fit to the net observed scattering profiles represented by the unfilled circles. The best-fit determined the values of $R_{g,u}$ and $R_{g,l}$ to be 1.6 μm and 29 nm, respectively, $p_3 = 3.7 \pm 0.05$, $D_m = 2.45 \pm 0.05$, and $D_s = 2.6 \pm 0.05$ (refer to Table 4).

IV-1.3. Comparisons between CB/Air and CB/Toluene

We compare the dispersion structures of CB particles in the pelletized powder (CB/Air) with those in toluene (CB/Toluene(20)). As previously described in section III-1, CB/Toluene(20) was prepared by grinding the pelletized powder in air and subsequently dispersing the grinded powder into toluene in the ultrasonic field. Thus, we expect that CB/Toluene(20) will build up the finest possible dispersion of the CB filler particles. As shown in Table 4, CB/Toluene (20) has $R_{g,l} = 21$ nm and $D_m = 2.6$, whereas CB/Air has $R_{g,l} = 24$ nm and $D_m = 2.5$, which indicates that small clusters with small $R_{g,l}$s build up compact MFAs with large D_m's, as observed in CB/Toluene(20), and large clusters with large $R_{g,l}$s build up loose or open MFAs with small D_m, as observed in CB/Air. This rule was universally demonstrated for other filler particles/polymer systems [6].

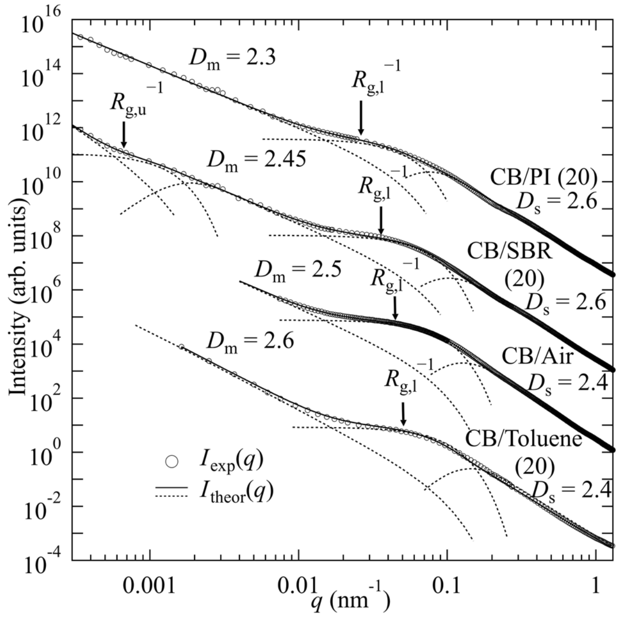

Fig. 7 Comparison of the combined SAS profiles for CB/PI(20), CB/SBR(20), CB/Air, and CB/Toluene(20). Each profile was vertically shifted to avoid overlaps

An average number of the primary particles N_P, which comprises the building blocks, may be estimated by $N_P \cong (R_{g,l}/R_{g,P})^3 = (21/10)^3 \cong 9$ if the building blocks are spheres. $R_{g,P}$ is the radius of the primary particle estimated by $R_{g,P} = \sqrt{3/5}R_{\mathrm{TEM}}$, where R_{TEM} (=13 nm) is the radius of the primary particle measured by TEM. We assume that the building blocks of MFAs in CB/Toluene(20) are the aggregates, in which approximately nine primary particles are fused as the smallest possible structural units for the dispersion of the CB fillers in the medium of polymer melts, toluene, or air. The aggregates are unbreakable units for further compounding the process of the fillers with polymers. Thus, $R_{g,l}$ in CB/Toluene(20) defined by $R_{g,l\text{,CB/Toluene(20)}}$ has a special meaning given by

$$R_{g,l,\mathrm{CB/Toluene(20)}} \equiv R_{g,\mathrm{agg}}, \tag{7}$$

where $R_{g,agg}$ is defined as the average radius of gyration of the CB aggregates, viz., the building blocks and the clusters are identical to the aggregates in the case of CB/Toluene (20). If the aggregates are spherical, their average radius is given by $R_{s,\mathrm{agg}} = \sqrt{5/3}R_{g,\mathrm{agg}} = 27\,\mathrm{nm}$.

The cluster of CB/Air has $R_{g,l} = 24$ nm, which is slightly larger than $R_{g,agg} = 21$ nm (Table 4). As a plausible model, we may assume that the building blocks of the MFAs for CB/Air comprise a mixture of dimers and unimers of the aggregates, which are statistically and randomly placed along the MFAs with a weight fraction of w_2 and $1 - w_2$, respectively. The average $R_{\mathrm{g},1}$ for CB/Air is given by

$$\left(R_{\mathrm{g},1}\right)^2_{\mathrm{CB/Air}} = w_2 R^2_{\mathrm{g,agg},2} + (1 - w_2) R^2_{\mathrm{g,agg},1}. \tag{8}$$

$R_{\mathrm{g,agg},2}$ and $R_{\mathrm{g,agg},1}$ are the radius of gyration of the dimer and that of the unimer, respectively. If the dimer is composed of two spherical aggregates with radii equal to $R_{\mathrm{s,agg}}$, which are in contact each other, then

$$R^2_{\mathrm{g,agg},2} = (8/5) R^2_{\mathrm{s,agg},1}, \quad R^2_{\mathrm{g,agg},1} = (3/5) R^2_{\mathrm{s,agg}}, \tag{9}$$

From Eqs. (8) and (9) with $R_{\mathrm{s,agg}} = 27$ nm and $(R_{\mathrm{g},1})_{\mathrm{CB/Air}} = 24$ nm (Table 4), we obtain $w_2 = 0.19$. In this case, approximately 20 wt% of the clusters in the MFAs are the dimers of the aggregates bonded by the inter-aggregate attractive interactions.

IV-2. Hierarchically self-organized CB fillers

Figure 7 summarizes the combined small-angle scattering profiles from the CB fillers dispersed in the various media, such as PI, SBR, air, and toluene in the double logarithmic scales, where the intensity scale in each scattering profile was vertically shifted to avoid overlapping. Note that the value ${R_{\mathrm{g},1}}^{-1}$ systematically increases in order from the top profile to the bottom profile. Thus, the size of the clusters $R_{\mathrm{g},1}$, which build up the MFAs, decreases in this order (refer to Table 4). The smallest cluster observed in toluene is expected to be the aggregates of the fused primary particles.

$(R_{\mathrm{g},1})_{\mathrm{CB/SBR(20)}}$ (=29 nm), which is defined as $R_{\mathrm{g},1}$ for CB/SBR(20) (refer to Table 4), is smaller than the average radius of gyration for the dimers of the aggregates $R_{\mathrm{g,agg},2} = \sqrt{8/5} \times 27\,\mathrm{nm} \cong 34$ nm, as calculated from Eq. (9). Thus, this cluster may also be a mixture of the unimers and the dimers of the aggregates. The fraction of dimers $w_2 \cong 0.55$ is estimated from Eqs. (8) and (9). $(R_{\mathrm{g},1})_{\mathrm{CB/PI(20)}}$ (=40 nm) which is defined as $R_{\mathrm{g},1}$ for CB/PI(20) (refer to Table 4) is larger than $R_{\mathrm{g,agg},2}$. Thus, the clusters for CB/PI (20), which are the largest clusters, are probably composed of a mixtures of the trimers, dimers, and unimers of the aggregates. A linear trimer of the spherical aggregates, in which the aggregates with the radius $R_{\mathrm{s,agg}}$ are in contact, has the largest radius of gyration $R_{\mathrm{g,agg},3} = \sqrt{49/15 R_{\mathrm{s,agg}}} \cong 49$ nm among other types of trimers.

The larger cluster tends to build up the larger MFAs with the larger upper cut-off size $R_{\mathrm{g,u}}$, as shown in Table 4 and Fig. 7, viz.,

$$\left(R_{\mathrm{g,u}}\right)_{\mathrm{CB/SBR(20)}} < \left(R_{\mathrm{g,u}}\right)_{\mathrm{CB/PI(20)}}, \tag{10a}$$

when

$$\left(R_{\mathrm{g},1}\right)_{\mathrm{CB/SBR(20)}} < \left(R_{\mathrm{g},1}\right)_{\mathrm{CB/PI(20)}}, \tag{10b}$$

and a more open or looser mass-fractal structure with a smaller D_{m},

$$\left(D_{\mathrm{m}}\right)_{\mathrm{CB/PI(20)}} < \left(D_{\mathrm{m}}\right)_{\mathrm{CB/SBR(20)}}. \tag{11}$$

The relationship given by Eqs. (10b) and (11) was universally found for CB/Toluene(20) and CB/Air as well.

Regarding the surface fractal dimension,

$$\begin{aligned} &\left(D_{\mathrm{s}}\right)_{\mathrm{CB/PI(20)}} = \left(D_{\mathrm{s}}\right)_{\mathrm{CB/SBR(20)}} = 2.6 > \\ &\left(D_{\mathrm{s}}\right)_{\mathrm{CB/Air}} = \left(D_{\mathrm{s}}\right)_{\mathrm{CB/Toluene(20)}} = 2.4. \end{aligned} \tag{12}$$

Therefore, the aggregate surfaces of CB/PI(20) and CB/SBR(20) after cross-linking is rougher than those of the pure CB powder. Their physical origin is discussed in Section IV-5.

Figure 8 presents the self-organized hierarchical structure of the CB fillers in toluene, CB/Toluene(20) (part a), and the crosslinked rubbers CB/SBR (20) and CB/PI(20) (part b), as elucidated by the analyses of the CSAS. Note that CB/Air has the same hierarchical structure as that shown in part (b), with the exception that the matrix of the filler particles is air instead of polymers and the aggregates in the clusters are bound only by the aggregate–aggregate attractive interactions in air.

The smallest dispersion unit of the fillers is the aggregate shown in (a-2) and (b-2), which comprise approximately nine fused primary particles. If we define the primary particle as the hierarchical structure level 1, then the aggregate is the structure level 2. The primary particle has the surface fractal structure and the internal structure characterized by the two-phase structure of the graphite crystallites and the amorphous phase (the turbostratic structure), as schematically shown in (a-1). The surface fractal dimension D_{s} of the fillers in air and toluene differ from that in the rubbers, as shown in (a-1) and (b-1) and summarized in Table 4, respectively. In the case of CB/Toluene(20), the aggregates serve as the building blocks, i.e., clusters, for the MFAs (the structure level 3), as schematically illustrated in part (a-3), which are dispersed in bulk fillers in toluene, as illustrated in (a-4) (the structure level 4).

In the case of the CB fillers in the rubbers, MFAs are not built up by the aggregates but are built up by the clusters, which are composed of a mixture of unimers, dimers, and trimers of the aggregates bound by network chains in the rubbers and attractive inter-aggregate

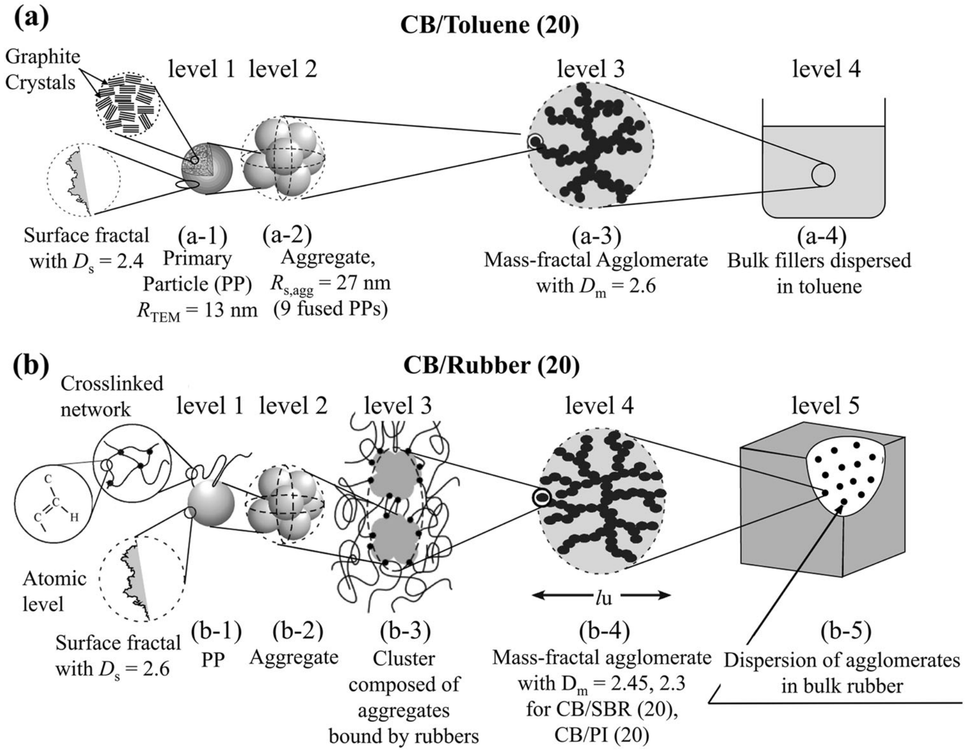

Fig. 8 Schematic of the hierarchically self-organized structure in CB/Toluene(20) (part a) and CB/SBR(20) or CB/PI(200) (part b). CB/Air has the same structure as those shown in part (b), with the exception that the matrix is air instead of the polymers. The structure in CB/Toluene (20) consists of the hierarchy level 1 to level 4, as shown in part (a-1) to part (a-4), respectively, whereas that in CB/SBR(20) or CB/PI(20) consists of the hierarchy level 1 to level 5, as shown in part (b-1) to part (b-5), respectively. In the former case, the aggregates (level 2 shown in part a-2) directly build up the mass-fractal agglomerate (level 3 shown in part a-3), whereas, the clusters (level 3 shown in part b-3) composed of the aggregates (level 2 shown in part b-2) build up the mass-fractal agglomerates (level 4 shown in part b-4) in the latter case

interactions in the medium of the rubbers, as schematically shown in parts (b-2) to (b-4). The clusters and MFAs correspond to the hierarchical structure level 3 and hierarchical structure level 4, respectively. The mass-fractal agglomerates are dispersed in the bulk CB/rubber compounds, as shown in part (b-5) (structure level 5), where the centers of the MFAs are schematically presented by dots. The MFAs formed in CB/Air are also built up by the clusters, of which a fraction is composed of the dimers of the aggregates that are physically bonded by the inter-aggregate attractive interaction in air and a fraction is composed of the unimers of the aggregates, i.e., the aggregate.

IV-3. Partially interdigitating mass-fractal agglomerates

How are the MFAs spatially distributed in the bulk filler/rubber compounds? This problem was explored by one of the authors of this paper; the study elucidated the concept of the partially interdigitating MFAs in space [21]. We will extend the fractal analysis.

Define $N_{\mathrm{cluster}}(r)$ as the number of the clusters with radius $R_{\mathrm{s,cluster}}$ that are enclosed in a sphere of radius r from the center O taken at a given cluster within the MFA with the dimension D_{m}, as defined in Fig. 9a, b. $N_{\mathrm{cluster}}(r)$ is given by

$$N_{\mathrm{cluster}}(r) = \left(r/R_{\mathrm{s,cluster}}\right)^{D_{\mathrm{m}}}. \tag{13}$$

The volume fraction of the clusters that exist within the part of the MFA $\phi_{\mathrm{cluster}}(r)$ is given by

$$\phi_{\mathrm{cluster}}(r) = N_{\mathrm{cluster}}(r)\left(\frac{R_{\mathrm{s,cluster}}}{r}\right)^{3} = \left(\frac{R_{\mathrm{s,cluster}}}{r}\right)^{3-D_{\mathrm{m}}}, \tag{14}$$

which decreases with an increase in r if $D_{\mathrm{m}} < 3$. The volume fraction of the cluster in the MFA with the upper cut-off radius of sphere R_{uc}, which is defined by $\phi_{\mathrm{cluster,MF}}$, is given by

$$\phi_{\mathrm{cluster,MF}} = \phi_{\mathrm{cluster}}(r = R_{\mathrm{uc}}). \tag{15}$$

This $\phi_{\mathrm{cluster,MF}}$ is related to the prescribed volume fraction of the filler particles in the compound and the volume fraction of the MFAs in the bulk compounds to be defined by ϕ_{CB} and ϕ_{MF}, respectively, as well as the volume fraction

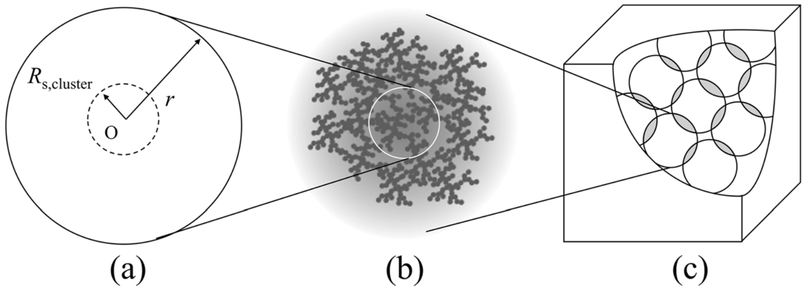

(a) Part of the MFA enclosed in sphere of radius r drawn from the center O of a cluster with radius $R_{\mathrm{s,l}}$.

(b) MFA

(c) Bulk composites composed of partially interdigitating MFA

Fig. 9 **a** Part of the mass-fractal agglomerate enclosed in a sphere of radius r with its center O taken at the center of a given cluster with radius $R_{\mathrm{s,cluster}}$ within the mass-fractal agglomerate (MFA); **b** an MFA with the upper cut-off radius R_{uc}; **c** bulk composites composed of partially interdigitating MFAs with R_{uc}. The shaded regions schematically illustrate the partial interdigitation of the MFAs

of the filler particles in the cluster $\phi_{\mathrm{p,cluster}}$, as a consequence of the hierarchical structure shown in Fig. 8b.

$$\phi_{\mathrm{CB}} = \phi_{\mathrm{MF}}\phi_{\mathrm{cluster,MF}}\phi_{\mathrm{p,cluster}} \cong \phi_{\mathrm{cluster,MF}}. \tag{16}$$

The second line in Eq. (16) assumes that ϕ_{MF} and $\phi_{\mathrm{p,cluster}}$ are not substantially smaller than unity; therefore, ϕ_{CB} and $\phi_{\mathrm{cluster,MF}}$ are in the same order.

From Eqs. (14) and (15), $\phi_{\mathrm{cluster,MF}}$ is given by

$$\phi_{\mathrm{cluster,MF}} = \left(R_{\mathrm{s,cluster}}/R_{\mathrm{uc}}\right)^{3-D_m}. \tag{17}$$

If the MFAs have the prescribed composition of the CB fillers in bulk ($\phi_{\mathrm{CB}} = 0.2$), how large should R_{uc} or $R_{\mathrm{g,u}}$ be? This answer can be obtained from Eqs. (16) and (17)

$$R_{\mathrm{uc}} = R_{\mathrm{s,cluster}}\left(\phi_{\mathrm{MF}}\phi_{\mathrm{p,cluster}}/\phi_{\mathrm{CB}}\right)^{1/(3-D_{\mathrm{m}})} \cong R_{\mathrm{s,cluster}}\phi_{\mathrm{CB}}^{-1/(3-D_{\mathrm{m}})}. \tag{18}$$

The second line of Eq. (18) is based on the assumption introduced in the second line of Eq. (16).

When Eqs. (17) and (18) are applied to the MFAs in CB/SBR(20) and CB/PI(20), we can deduce the following results:

(1) In the case of CB/SBR(20), $R_{\mathrm{s,cluster}} = \sqrt{5/3}\, R_{\mathrm{g,1}} = \sqrt{5/3} \times 29 = 37.4\,\mathrm{nm}$ and $D_{\mathrm{m}} = 2.45$ from Table 4. From the second line of Eq. (18), $R_{\mathrm{uc}} = 37.4 \times 0.2^{-1/0.55} = 698\,\mathrm{nm}$, and $R_{\mathrm{g,u}} = 540\,\mathrm{nm}$. The estimated value $R_{\mathrm{g,u}}$ is considerably smaller than the experimentally assessed value of $R_{\mathrm{g,u}} = 1.6\,\mu\mathrm{m}$ based on the CSAS method. If we consider the factor $(\phi_{\mathrm{MF}}\phi_{\mathrm{P,cluster}})^{1/0.55} < 1$, R_{uc} and $R_{\mathrm{g,u}}$ become smaller than the above cited values, e.g., by a factor of ~1/2 when $\phi_{\mathrm{MF}}\phi_{\mathrm{p,cluster}}$ ~2/3. If the MFAs have $R_{\mathrm{g,u}} = 1.6\,\mu\mathrm{m}$, as analyzed by the CSAS method and shown in Table 4, the theoretical value of $\phi_{\mathrm{CB}} \cong \phi_{\mathrm{cluster,MF}}$ is estimated from Eqs. (16) and (17).

$$\phi_{\mathrm{CB}} \cong \phi_{\mathrm{cluster,MF}} = \left(\frac{R_{\mathrm{s,cluster}}}{R_{\mathrm{uc}}}\right)^{3-D_{\mathrm{m}}} = \left(\frac{R_{\mathrm{g,1}}}{R_{\mathrm{g,u}}}\right)^{0.55} = \left(\frac{29}{1600}\right) \cong 0.11 = 11\%.$$

This value is considerably smaller than 20%. This finding suggests that the mass-fractal agglomerates with $R_{\mathrm{g,u}} = 1.6\,\mu\mathrm{m}$ and $D_{\mathrm{m}} = 2.45$ in CB/SBR(20) is an open structure with a small value of D_{m}; thus, they must be partially interdigitated to ensure that $\phi_{\mathrm{CB}} = 0.2$, as schematically illustrated in Fig. 9c, where the circles designate the MFAs with R_{uc} and the overlapped parts of the circles schematically illustrate the interdigitated regions of the MFAs.

(2) In the case of CB/PI(20), $R_{\mathrm{g,l}} = 40\,\mathrm{nm}$ and $D_{\mathrm{m}} = 2.3$ (Table 4). Thus, the theoretical R_{uc} based on the second line in Eq. (18) gives

$$\begin{aligned} R_{\mathrm{uc}} &= (1/0.2)^{1/(3-2.3)} 40\sqrt{5/3} = 514\,\mathrm{nm}, \\ R_{\mathrm{g,u}} &= 514\sqrt{3/5} = 398\,\mathrm{nm}. \end{aligned} \tag{19}$$

This value is substantially smaller than the $R_{\mathrm{g,u}}$ (>2 μm) obtained from the analysis of the experimental CSAS (Table 4). The MFAs in CB/PI(20) have an open structure with a small D_{m}; thus, they must be partially interdigitated as shown in Fig. 9c.

IV-4. Anisotropy in the shape of the clusters

The analyses in Sections IV-1.3 and IV-2 regarding the clusters that build up MFAs in CB/Air, CB/SBR(20), and CB/PI(20) revealed that the shape of the clusters was anisotropic, despite the fact that the analyses based on the UFGPA quantitatively determined only the radius of

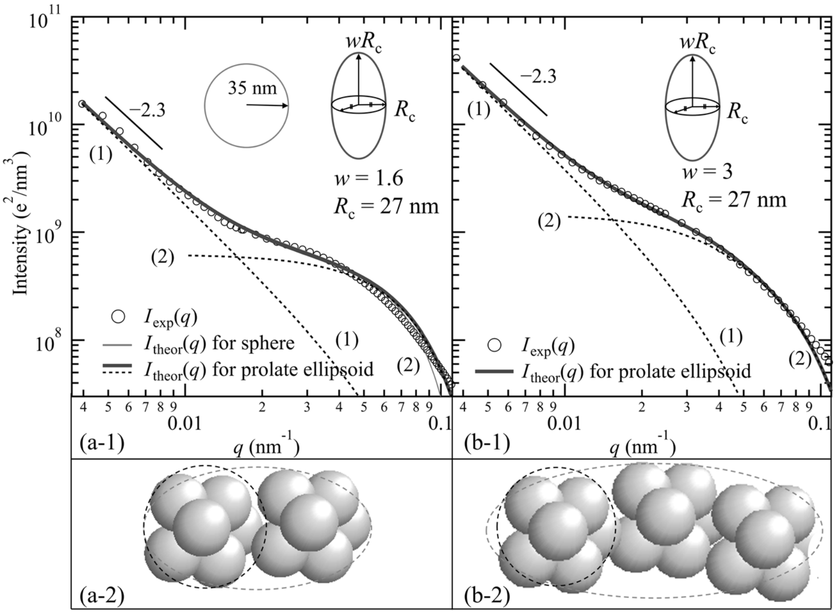

(a) CB/SBR (20) (b) CB/PI (20)

Fig. 10 Expanded view of the USAXS profiles focused on the q-range between 0.004 and 0.1 nm^{-1} for (a-1) CB/SBR(20) and (b-1) CB/PI (20) [$I_{\mathrm{exp}}(q)$] shown by symbols. In part (a-1), $I_{\mathrm{exp}}(q)$ was best-fitted with the theoretical profile based on the modified UFGPA $\overline{I_{theor}(\mathrm{q})}$ (Eq. (24)) using $\overline{F(q)}$ for a sphere with a polydispersity in its radius (red solid line or solid line) and an ellipsoid of revolution (blue line or thick solid line). In part (b-1), $I_{\mathrm{exp}}(q)$ was best-fitted with $I_{\mathrm{theor}}(q)$ for an ellipsoid of revolution (blue solid line or solid line). The broken lines numbered (1) and (2) show the contributions of the first term and the second term in rhs of Eq. (24) to the net $I_{\mathrm{theor}}(q)$, respectively. The parts (a-2) and (b-2) present the ellipsoid models and corresponding dimer and trimer of the aggregates having the same $R_{\mathrm{g,cluster}}$

gyration of the clusters $R_{\mathrm{g,1}}$. The anisotropy was indirectly unveiled by the comparison between the $R_{\mathrm{g,1}} \equiv R_{\mathrm{g,agg}}$ determined for CB/Toluene(20) and the $R_{\mathrm{g,1}}$s determined for CB/Air, CB/SBR(20), and CB/PI(20).

In this section, we directly elucidate the shape anisotropy of the clusters. In the UFGPA, information about the shape of the clusters remains unsolved because the Guinier scattering function [19] and $R_{\mathrm{g,1}}$ are independent of the shapes of the clusters. Therefore, we attempted to modify the UFGPA by replacing the Guinier function with the form-factor $F(q)$ of the clusters that have a plausible shape:

$$I(q) \cong A'[\exp(-R_{\mathrm{g,1}}^2 q^2/3)]q_{\mathrm{m}}^{-D_m} + B'F(q), \tag{20}$$

where A' and B' are proportionality constants. Note that the form factor displays the Porod law (power law of q^{-4}) in the high q-region (Region I) in the case of clusters with a smooth surface, whereas all experimental scattering profiles showed a deviation from the Porod law at $q > q_{\mathrm{s}} = 0.2\,\mathrm{nm}^{-1}$ due to the contribution of the surface fractal structure that exists on the surfaces of the clusters. Thus, the data analyses based on Eq. (20) were performed in the q-range at $q < 0.1\,\mathrm{nm}^{-1}$ to exclude the contribution from the surface fractal scattering observed at $q > q_{\mathrm{s}} = 0.2\,\mathrm{nm}^{-1}$. This approximation can also be derived from the treatment proposed by Sinha and coworker [15] regarding the cut-off problem for the power-law scattering curves.

First, we examined the size and shape of the aggregates in CB/Toluene(20) based on the assumption that the shape is spherical with the radius $R_{\mathrm{s,agg}}$. Thus, the form factor $F(q)$ is given by

$$F(q) \propto R_{\mathrm{s,agg}}^6 \Phi^2(u), \tag{21}$$

where

$$\Phi(u) = \frac{3}{u^3}(\sin u - u\cos u), \tag{22}$$

with $u = qR_{\mathrm{s,agg}}$. We considered the polydispersity of $R_{\mathrm{s,agg}}$ given by a Gaussian function:

$$P(R_{\mathrm{s,agg}}) \sim \exp\left[\left(R_{\mathrm{s,agg}} - \overline{R}_{\mathrm{s,agg}}\right)^2/\left(2\sigma_{\mathrm{R}}^2\right)\right], \tag{23}$$

where $\overline{R}_{s,agg}$ and σ_{R} are the average $R_{\mathrm{s,agg}}$ and the corresponding standard deviation, respectively.

The averaged scattering intensity $\overline{I_{theor}(\mathrm{q})}$ is given by

$$\overline{\mathrm{I_{theor}}(q)} \cong A'[\exp(-R_{\mathrm{g,1}}^2 q^2/3)]q^{-D_{\mathrm{m}}} + B'\overline{F(q)}, \tag{24}$$

Table 5 Structural parameters that characterize the clusters based on the modified UFGPA

Parameters[a]	$(R_c)_K$[b] (nm)	w_K[b]	$(R_{g,cluster})_K$[c] (nm)	$(N_{agg})_K$[d] per cluster
Sample K				
CB/SBR (20)	27	1.6	28	1.6
CB/PI (20)	27	3.0	42	3.0
CB/Toluene (20)	27[e]	1.0	21	1

[a] Structural parameter obtained for sample K, where K = CB/SBR (20), CB/PI (20), or CB/Toluene (20).

[b] $(R_c)_K$ and w_K are the parameters that characterize the prolate ellipsoid of revolution with the half axial length $[(R_c)_K, w_K(R_c)_K]$ assumed for the anisotropic shape of the clusters, which build up the mass-fractal agglomerates.

[c] $(R_{g,cluster})_K$ is the radius of gyration of the anisotropic clusters for the sample K as calculated by $(R_{g,cluster})_K{}^2 = [(2+w_K{}^2)/5](R_c)_K{}^2$.

[d] $(N_{agg})_K$ is the average number of the aggregates incorporated in the clusters given by Eq. (28).

[e] In the case of CB/Toluene (20), the clusters are identical to the aggregates; thus, $R_c = R_{s,agg}$, viz., the average radius of the clusters is identical to that of the spherical aggregates.

where $\overline{F(q)}$ is the average form factor given by

$$\overline{F(q)} = \int_0^\infty P(R_{s,agg}) R_{s,agg}^6 \Phi^2(u; R_{s,agg}) dR_{s,agg} \Big/ \int_0^\infty P(R_{s,agg}) dR_{s,agg}, \qquad (25)$$

and $R_{g,l}$ in Eq. (24) is given by $R_{g.1} = \sqrt{3/5} R_{s,agg}$. $\overline{I_{theor}(q)}$ given by Eqs. (24) and (25) with $D_m = 2.60 \pm 3$, $\overline{R}_{s,agg} = 27 \pm 3$ nm, and $1 < \sigma_R < 5$ nm successfully fit the scattering data for CB/Toluene(20) at $0.04 < q \leq 0.1$ nm^{-1} [although the fitting result is not shown here (refer to ref. [2] for the fitting result)]. The fitting result was as good as that attained in the case where the Guinier function with $R_{g,l} = 21$ nm is used for $\overline{F(q)}$, as shown for CB/Toluene(20) in Fig. 2. We, therefore, conclude that the aggregates observed after sonification of the grinded fine CB powder in the toluene solution are spherical.

Second, following the same treatment with Eq. (24), we analyzed the form factors of the clusters in the rubbers. We fitted the data for CB/SBR(20) based on the assumption that the shape of the cluster was spherical: $F(q)$ and $\overline{F(q)}$ for the clusters can be expressed by Eqs. (21) and (25), respectively, with substitution for $R_{s,agg}$ with the radius of the cluster $R_{s,cluster}$. As shown in Fig. 10(a-1), the best-fitted scattering profile for the spherical model with $\overline{R}_{s,cluster} = 37 \pm 6$ nm and $10 < \sigma_R < 15$ nm (solid red line or thin solid line) using Eqs. (24) and (25) can satisfy the experimental profile (unfilled circles) up to $q \cong 0.05$ nm^{-1}: at $q > 0.005$ nm^{-1}, the $I_{theor}(q)$ deviates downward from the $I_{exp}(q)$.

To consider the deviation from the spherical model at $0.05 < q < 0.1$ nm^{-1}, we assumed that the shape of the cluster was an ellipsoid of revolution. The scattering intensity from the ellipsoid of revolution with the radii (R_c, R_c, wR_c) with a random orientation is given as follows:

$$\overline{F(q)} = (4\pi w R_c^3/3)^2 \int_0^\pi \Phi^2(u) \sin\beta d\beta, \qquad (26)$$

where u is defined by

$$u \equiv qR_c\left[\sin^2\beta + w^2\cos^2\beta\right]^{1/2}. \qquad (27)$$

Here, w and β are an aspect ratio of the ellipsoid and a polar angle between the axis of revolution and the reference axis, respectively. In this case, $R_{g,l}$ in Eq. (24) is given by $R_{g,l} = R_c[(2+w^2)/5]^{1/2}$. As shown in Fig. 10(a-1), the ellipsoid model with $R_c = 27.4 \pm 0.5$ nm and $w = 1.6 \pm 0.2$ shows a reasonable fit to the data (open circles) up to $q = 0.09$ nm^{-1} [blue solid line (or thick solid line)] calculated by Eqs. (24) and (26)]. The results are also listed in Table 5. Note that consideration of the polydispersity of the radii of the ellipsoids, which is disregarded in the present analysis, can further reduce the small deviation between the observed profile and the calculated profile.

Third, the modified UFGPA was also applied to CB/PI (20). We confirmed that the spherical model for the cluster with $\overline{R}_{c,cluster}$=52 ± 6 nm and $4 < \sigma_R < 10$ nm can only fit the experimental profile up to $q = 0.05$ nm^{-1} as in the case of CB/SBR(20) shown in Fig. 10(a-1) (although the fitting result is not shown here). Similar to the case of CB/SBR (20), we adopted the ellipsoid model for the CB cluster in the PI matrix. As shown in Figs. 10(b-1), the ellipsoidal model was able to fit the data up to $q = 0.09$ nm^{-1}, and the corresponding R_c and w values were estimated to be $R_c = 27.4 \pm 0.5$ nm and $w = 3.0 \pm 0.3$, respectively (Table 5).

Thus, the findings revealed that the CB clusters in the SBR matrix are more compact with the smaller shape anisotropy, whereas those in the PI matrix are more extended with the larger shape anisotropy even for the same compounding condition. Note that the findings are consistent with those in TEMs (Fig. 4b, d). This result may imply the disparity in the effective attractive interaction between the aggregate and the polymer in the two systems. Although these two polymers differ with regard to the molecular weight, the molecular weight affects the effective interaction of CB per polymer chain and the rate of the cluster formation and the MFA formation, because T_g is almost identical for SBR and PI (Table 1).

The structural parameters of the clusters, which are characterized by the modified UFGPA, are summarized in Table 5 based on the ellipsoid of the revolution model. The estimated parameters, such as $(R_{g,cluster})_K$ and $(D_m)_K$, are

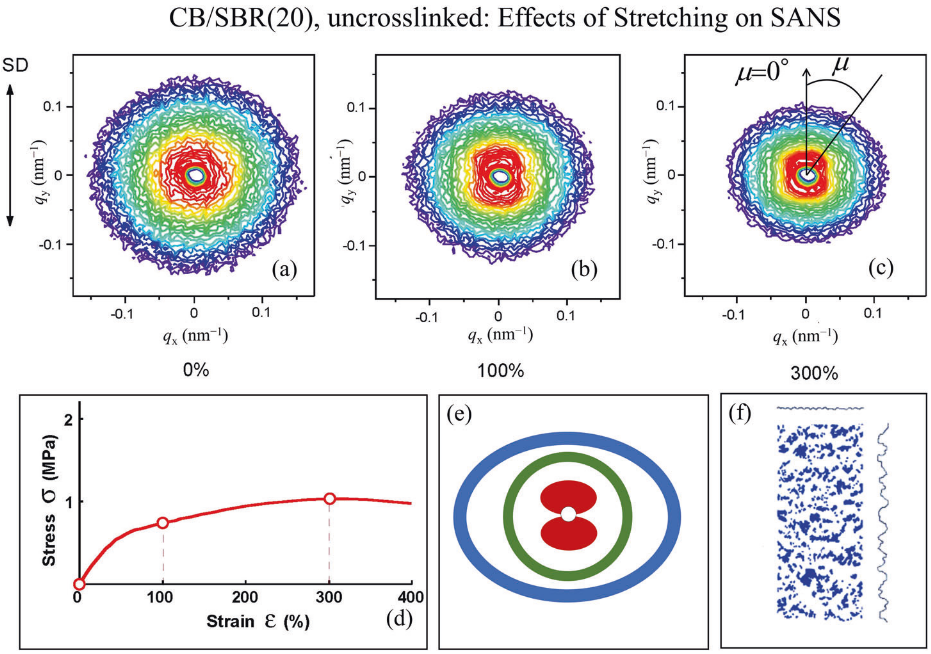

Fig. 11 Change in 2D SANS pattern after stretching the un-crosslinked CB/SBR(20) sheets by **a** 0%, **b** 100%, and **c** 300%, where the stretching direction (SD) is vertical. Part **d** shows the stress vs. strain curve taken at room temperature; part **e** shows a schematic of the q-dependent anisotropic SANS patterns for the stretched sheets; and part **f** shows anisotropic density fluctuations of the filler particles developed in the stretched sheets

consistent with those characterized by UFPGA. However, the modified UFGPA provided the additional parameter that characterizes the shape of the cluster w_K and the parameter $N_{agg,K}$, viz., the average number of aggregates enclosed in the cluster, as listed in Table 5 and schematically illustrated in (a-2) and (b-2) in Fig. 10. $(N_{agg})_K$ was estimated based on the following equation:

$$\frac{4\pi}{3} w_K \left(R_c^3\right)_K = \frac{4\pi}{3} R_{s,agg}^3 (N_{agg})_K, \text{ viz.}, (N_{agg})_K = w_K \qquad (28)$$

Note that we define $(R_c)_K$ as satisfying $(R_c)_K \equiv R_{s,agg}$. The value N_{agg} evaluated is consistent with the analysis in Section IV-2 with respect to w_2 (weight fraction of the dimers of the aggregates in the cluster for CB/SBR(20)) based on UFGPA. If the weight of the aggregate is defined as W_{agg}, then N_{agg} for the cluster in CB/SBR(20) satisfies $N_{agg} W_{agg} = 2W_{agg} w_2 + W_{agg}(1 - w_2)$. Thus,

$$N_{agg} = 1 + w_2 = 1.55$$

The shape anisotropy of the clusters can be confirmed by investigating two-dimensional (**2D**) SAS patterns from the deformed samples, because the 2D patterns become anisotropic if the anisotropic clusters are oriented in the deformation. Figure 11 shows the 2D SANS patterns at room temperature for the un-crosslinked CB/SBR(20) sheets (a) before stretching, (b) after stretching by 100% and (c) 300%, where the stretching direction (SD) is vertical, as shown in the figure. The specimens were stretched to the given elongational strain (ε) at room temperature. The stretched specimens were immediately fixed at the given ε and allowed to relax the stress at the fixed strain [21]. The 2D patterns in (b) and (c) were taken at 3000 s after the stretching and fixing. Part (d) shows the stress (σ) and strain (ε) curve of the specimen at room temperature. The unstretched specimen presents a circularly symmetric pattern with its q-dependence shown in Fig. 4a; thus, the hierarchically self-organized structures are randomly oriented in 3D space.

The scattering patterns became increasingly anisotropic with an increasing ε in the two aspects (1) and (2) to be detailed below. Moreover, the anisotropy of the pattern developed at the given ε was observed to increase with an increase in the relaxation time after stretching to the given constant ε (via the trend that is not shown here). This finding reveals that the dissipation process of the energy imposed to samples during the stress relaxation time creates the following flow-induced characteristic patterns (1) and (2):

(1) At the large q in Region II (shown in Fig. 5), the 2D scattering patterns tend to have an elliptical shape that extends more along $\mu = 90°$ than along $\mu = 0°$, where μ is the azimuthal angle defined in part (c), as shown by the blue-colored iso-intensity contour lines and illustrated by the schematic pattern in part (e).

(2) At the small q in Region III (shown in Fig. 5), the 2D scattering patterns tend to exhibit butterfly patterns [22, 23], which are characterized by the red "wings" with high scattering intensity along $\mu = 0°$ and the twofold symmetry will respect to the equator at $\mu = 90°$, as shown in parts (b) and (c) and illustrated by the schematic pattern shown in red color in part (e).

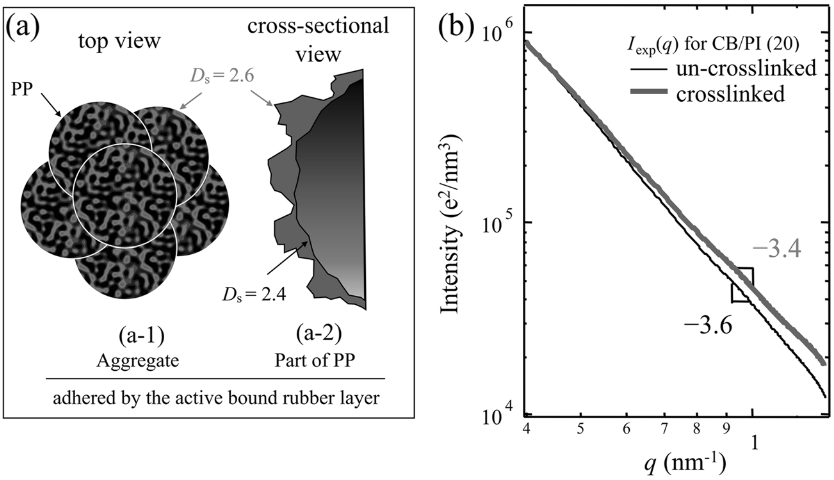

Fig. 12 **a** The aggregate composed of the fused primary particles (PP) (part a-1) and a part of PP (part a-2), in which the active bound rubber layer (illustrated by red parts) is adhered to the PP surface. **b** SAXS profiles for crosslinked (red line, thick line) and un-crosslinked (black solid line, thin solid line) sheets of CB/PI(20)

The crossover of the opposite μ-dependence of the red pattern and blue pattern in Region III and Region II, respectively, develop the circularly symmetric green patterns shown in parts (b), (c) and (e) in the q-region, where the crossover occurs.

(1) The blue elliptical pattern extended along $\mu = 90°$ is a consequence of the long axes of the anisotropic clusters being oriented parallel to the SD.
(2) The red butterfly pattern extended along $\mu = 0°$ is a consequence of the flow-induced spatial density fluctuations of the filler particles in the rubber matrix along the SD, as schematically shown in part (f), where the blue and bright regions are regions rich in filler particles and lean in filler particles, respectively. The density fluctuations are large and small along the direction parallel and perpendicular to the SD, respectively, with respect to the spatial extension of the fluctuations, as illustrated by the wavy patterns drawn on the right-hand side and top of part (f), respectively.

IV-5. Roughened filler surface via formation of bound rubber layer

We have elucidated that the cross-linked CB/PI(20) and CB/SBR(20) have a larger surface fractal dimension ($D_s = 2.6$) than CB/Air and CB/Toluene ($D_s = 2.4$), as shown in Table 4 and Figs. 7 and 8. This finding suggests that the roughness of the CB aggregates is enhanced in the cross-linked SBR and PI matrices. Since the surface of the aggregate itself would not utterly change with the cross-linking reaction of SBR and PI at 170 °C, the enhanced surface roughness after the cross-linking is a consequence of the formation of the bound layer [24–26] of SBR and PI on the aggregate surface, the surface roughness of which may enhance the net D_s cooperatively with the self-similar surface roughness of the aggregates adhered by the bound layer, as schematically illustrated in Fig. 12a. We shall designate this bound layer as an "active bound layer".

Figure 12b focuses on the effects of the cross-linking of matrix polymer on the SAXS profiles in the high q-range of Region I. The scattering profiles from CB/PI(20) before and after cross-linking PI are represented by the solid black line (thin line) and the solid red line (thick line), respectively. The power-law exponent $p_1 = 3.6$ and the surface fractal dimension $D_s = 2.4$ for the CB/PI(20) before cross-linking is identical to p_1 and D_s for pure CB, respectively. We are surprised to recognize the enhanced surface roughness of the CB filler particles only after the cross-linking of PI with the employed scattering method. To confirm the change in D_s before and after cross-linking for other filler/polymer systems also deserves future work. Nevertheless, this conclusion infers the following two plausible interpretations:

(1) The "active bound polymer layer" which is formed on the rough surfaces of the aggregates only after the cross-linking increases the net D_s to 2.6 cooperatively with the surface roughness of the bare CB with $D_s = 2.4$.
(2) The bound polymer layer may be formed even prior to cross-linking but it may not be detected by SAXS because the electron density of the layer prior to cross-linking may be much smaller than that of CB. In this sense, the bound polymer layer formed prior to cross-linking may not yet be the "active bound layer".

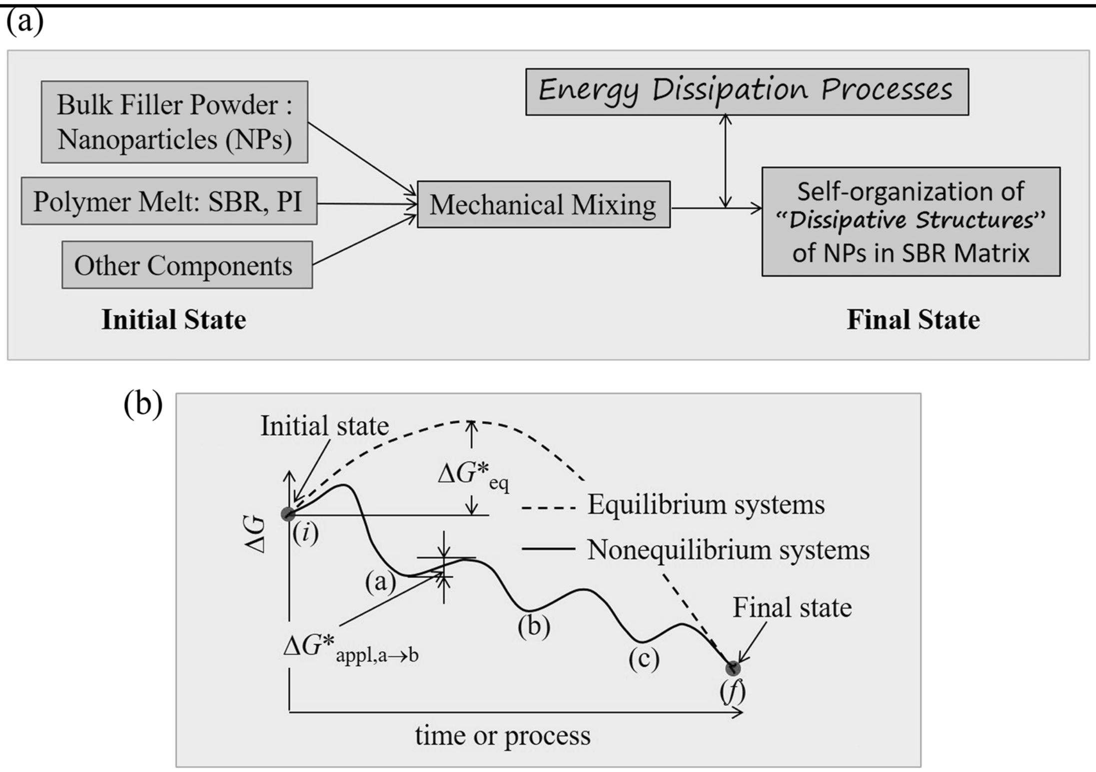

Fig. 13 **a** Self-organization in nonequilibrium systems composed of a bulk powder and a bulk polymer melt as an initial state to a final ordered state in applied mechanical field. **b** Free energy barriers for structural evolution from the initial state (*i*) to the final state (*f*) with and without the external fields schematically represented by a solid line and a broken line, respectively

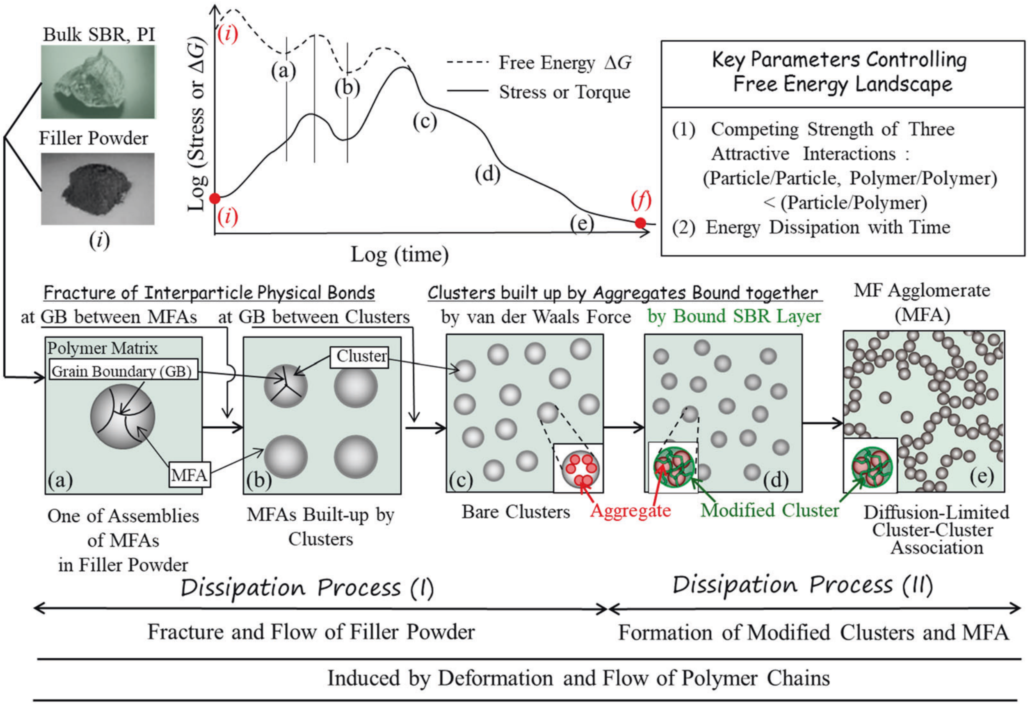

Fig. 14 Cascade evolution of the dissipative structures (**a**) to (**e**) accompanied by the energy dissipation processes [Process (I) and Process (II)], the relevant free energy landscape, the relevant changes in stress level, and controlling key parameters for given compounding conditions

In the case of (2), the electron density of the bound layer may become sufficiently larger relative to that of CB and that of the bulk rubber matrix only after cross-linking, so that the bound layer may become the "active" bound layer only after cross-linking. The cross-linking density in the bound polymer layer may be considerably higher than that in the bulk polymer matrix, which may infer an enrichment of the cross-linker liquid molecules around the rough aggregate surface prior to the cross-linking reaction. The investigation of this enrichment of the small liquid molecules around the self-similar rough surface of filler particles deserves future theoretical and experimental studies concerning the basic surface science. Figure 12a schematically illustrates the active bound PI layer adhered to the aggregate (part a-1, top view) and one of the primary particles in the aggregate (part a-2, cross-sectional view).

V. Self-organization mechanism in nonequilibrium systems: from dissipative structures to ordered structures through fluctuations, trapped eventually at nonequilibeium

V-1. Fundamental themes in physical science and engineering in nonequilibrium systems

Figure 13 presents the self-organization in the nonequilibrium system in applied mechanical fields. In an initial state, the system is composed of a bulk powder of the filler NPs and a bulk polymer melt as main components, as well as other components that are important for final products. The components in the system are mixed by applied mechanical fields to develop the self-organized filler NPs in the polymer matrix as a final state, as shown in part (a). During the mixing process, the mechanical energy imposed to the system is dissipated by various energy dissipation processes. Each energy dissipation process conceivably creates the corresponding dissipative structure, as shown in part (a). Even in the case where the free energy of the system ΔG at the initial state (i) is higher than that at the final state (f), as shown in part (b), this final state favored at thermodynamic equilibrium may not be necessarily achieved easily if the free energy barrier ΔG^*_{eq} for the transformation without the applied field is considerably larger than the thermal energy $k_\mathrm{B}T$.

In the applied filed, the free energy barrier ΔG^*_{eq} is expected to be substantially suppressed and to change into the free energy landscape, as schematically represented by a solid line for the cascade transformation from structure (i) to structure (f) via the formation of the dissipative structures (a) to (c), for example, as shown schematically in Fig. 13b. The free energy barriers for the cascade transformation of the structures from (i) to (a), (a) to (b), (b) to (c), and (c) to (f) (defined as $\Delta G^*_{\mathrm{appl},a\to b}$, etc.) would be considerably smaller than ΔG^*_{eq}, which enable the most stable final structure (f) with the lowest free energy to be achieved through the cascade transformation of the dissipative structures only with the existence of the external fields. Key fundamental problems to be solved in the self-organization of nonequilibrium systems are to clarify the free energy landscape and various cascade structures developed in various compounding conditions with various filler particle/polymer systems of various particle/particle, particle/polymer, and polymer/polymer attractive interactions.

V-2. Proposed self-organization mechanism via cascade evolution of dissipative structures

We elucidated the hierarchically self-organized CB filler particles in air, as demonstrated for CB powder (CB/Air), and in the rubber matrices, as observed for CB/SBR(20) and CB/PI (20). In this section, we discuss how the self-organized structure of CB particles in air are transformed into that in the polymer matrices. We propose a possible transformation process, which is schematically shown in Fig. 14.

The mixing of a bulk SBR or PI and a bulk CB filler powder, which exist in their initial state as shown in (*i*) in the figure, causes stress to build up (as shown by the solid line in the top center diagram). This stress breaks the powder, which is composed of a large number of assemblies built up by the MFAs, into a larger number of smaller assemblies of the MFAs dispersed in the polymer matrix. Figure 14a schematically presents only one of the many assemblies of the MFAs in the filler powder. This process serves to partially dissipate the mechanical energy imposed on the system and contributes to a stress relaxation. In the assembly of the MFAs, the MFAs are physically bonded by direct particle–particle attractive interaction in air through their grain boundaries (GB). The polymer chains have strong attractive interactions with the particles, which causes the chains to adhere to the surface of the assembly of the MFAs. The adhered chains may entangle with free chains or chains that are partly adhered to another assembly of the MFAs, which may increase the stress level of the system during deformation and flow of the matrix chains.

The built-up stress will further break the assembly of MFAs into individual MFAs, as shown by the process from (a) to (b), and the isolated MFAs are dispersed in the polymer matrix, as schematically shown in part (b). This process involves fractures of the particle–particle physical bonds at the GBs between the MFAs and serves to dissipate the mechanical energy imposed on the assembly of the MFAs, which causes the stress relaxation of the system. The evolution of the MFAs (b) from the assembly of the MFAs (a) will create new interfacial area on which new polymer chains are adhered. This process will again cause a buildup of the stress level in the system and the stress level imposed on the isolated MFAs, which are composed of the clusters that are physically bonded by the direct cluster–cluster attractive interaction in air at GBs, as schematically illustrated in part (b). The built-up stress may fracture the particle–particle physical bonds at the GBs between the clusters to break up the MFAs into individual clusters, as shown in the process from (b) to (c), which are dispersed in the polymer matrix, as illustrated in the part (c). The fracture process from (b) to (c) for the formation of the clusters contributes to the energy dissipation and stress relaxation.

The clusters are composed of aggregates that are bonded by aggregate–aggregate attractive interactions, as schematically shown in the inset to part (c). The surfaces of the aggregates and clusters that are newly developed immediately after the breakup of the MFAs, as shown in stage (c), are just exposed to the polymer matrix and thereby are free from the bound polymer layer adhered to the surfaces [24–26]. Thus, we shall designate the clusters in this stage (c) as “Bare Clusters”. As time elapses in the mixing process, the aggregates and the clusters are surrounded by the bound polymer layer due to a strong polymer–particle attractive interaction, as schematically shown in the inset to part (d). We designate the clusters in this stage (d) as “Modified Clusters” because the surfaces of the bare clusters in (c) are covered by the bound polymer layer and the aggregates within the clusters are bound by polymer chains. Thus, the nature of the clusters drastically change from the bare clusters (c) to the modified clusters (d), which also causes the energy dissipation and the stress relaxation of the system.

The bound polymer layer stabilizes the clusters (i) against the stress-induced breakup into the aggregates and (ii) against growth of the clusters, which is driven by the flow-induced diffusion-coalescence of the clusters, into large 3D compact structures with $D_{\mathrm{m}} \cong 3$ dispersed in the polymer matrix. The latter stabilization (ii) is due to the entropic repulsion of the chains in the layer. The modified clusters formed by the polymer–particle and particle–particle attractive interactions serve as stable dispersion units (clusters) that build up the MFAs, as shown in part (e), by the flow-induced diffusion-limited cluster–cluster aggregation, as shown in the process from parts (d) to (e). This process causes the energy dissipation and the stress relaxation of the systems.

The hierarchical self-organization in the nonequilibrium systems from the initial structure to the final structure occurs via the cascade evolution of the characteristic dissipative structures (a) to (e) as a consequence of the dissipation of the applied mechanical energy imposed on the systems. The energy dissipation processes in the entire self-organization process may be classified into the following two processes, as indicated at the bottom of Fig. 14: *Dissipation Process (I)* involves fracture and flow of powder of filler particles, which cause the cascade evolution of the finer dissipative structures of the powder, as shown in the process from (a) to (c). *Dissipation Process (II)* involves the first formation of the modified clusters dispersed in the polymer matrices (d) and subsequent formation of the MFA built up by the modified clusters (e). Both Dissipation Process (I) and Dissipation Process (II) are commonly induced by deformation and flow of SBR or PI chains. Dissipation process (I) directs the particles to attain maximum placement entropy to form the bare clusters. This process is rational because it reduces ΔG due to the gain of both the placement entropy increase and the enthalpy reduction driven by an increasing interfacial area between the particles and the polymers and an increasing number of attractive physical bonds between the polymers and the particles. Dissipation process (II) directs the clusters to order because it reduces the placement entropy of the modified clusters. The cost of the entropy reduction may be counter-balanced by the gain of the enthalpy reduction due to an increasing number of bondings between the modified clusters, which may cause a decreasing ΔG in this process. The ordering is eventually pinned at nonequilibrium by cross-linking of the matrix chains to form the final structure (f).

As schematically presented at the top center in Fig. 14, the cascade evolution of the dissipative structures (a) to (e) would be accompanied by the cascade reduction of the free energy of the system, as qualitatively shown by the broken line [broken line from (c) to (e) exhibits the same trend as the solid line from (c) to (e)] and the cascade change in the stress of the system with mixing time, as schematically shown by the solid line. The local minima (a) to (e) in ΔG and the stress may reflect the formation of the dissipative structures (a) to (e). The local maxima in ΔG correspond to the local free energy barrier $\Delta G^{*}_{appl,k\rightarrow l}$ for the transformation from the *k*-th to the *l*-th dissipative structure. The key parameters that control the free energy landscape may be (1) the competing strength of the three attractive interactions of particle–particle, polymer–polymer, and particle–polymer and (2) the energy dissipation with time, as indicated in Fig. 14 in the top right corner. For the competing interactions, we expect that the strength of particle–polymer is stronger than those of the other interactions.

VI. Concluding remarks

We have investigated hierarchically self-organized dissipative structures of the filler particles in the polymer matrices as one of general problems in physical science concerning self-organization in nonequilibrium systems that are open to external fields. Using a combined small-angle scattering method, we elucidated the self-organized structures of the carbon black NPs (CB) in poly(styrene-*ran*-butadiene) (SBR) and polyisoprene (PI) in the mesoscopic length scale that ranges from ~ nm to ~10 µm.

Based on these results and the relevant results elucidated on pure CB powder, we proposed that the hierarchical self-organization of the ordered mass-fractal agglomerates of the filler particles [as shown in Fig. 14e] is a consequence of the cascade evolutions of the characteristic dissipative structures [(a)–(e) shown in Fig. 14]: the evolution of each dissipative structure is accompanied by the characteristic energy dissipation process of the external mechanical energy applied to a given system. The entire dissipation process is classified into two processes: Dissipation Process (I) involves fracture and the flow of filler powder in polymer matrices to create the bare clusters that are individually dispersed in the matrices. Dissipation Process (II) involves the formation of the clusters that are adhered by the bound polymer layer (defined as the **modified clusters**) and subsequent formation of the mass-fractal agglomerates built up by the modified clusters. Both processes are commonly induced by deformation and flow of the matrix polymer chains. We proposed that the cascade evolution of the dissipative structures would involve the cascade reduction of the free energy barrier for the transformation from the initial structure to the final structure, which enables the structure formation that is not feasible in equilibrium systems without external fields imposed to systems. It deserves future work to clarify the free energy landscape and achieve an elaborate detection of the stress trajectory (shown in Fig. 14), for various compounding conditions with various filler particles and polymers that have various particle–particle, particle–polymer, and polymer–polymer interactions.

Acknowledgments We thank Drs. Tadanori Koga, Kazuya Aizawa, Masao Nakamura, Daisuke Yamaguchi, and Satoshi Koizumi for their contributions to this study via the work cited in ref. [2]. The synchrotron radiation experiments were performed at the second hutch of SPring-8 BL03XU (Frontier Softmaterial Beamline (FSBL)), which was constructed by the Consortium of Advanced Softmaterial Beamline.

Compliance with ethical standards

Conflict of interest The authors declare that they have no conflict of interest.

References

1. Nikolis G, Prigogine I. Self-Organization in Nonequilibrium Systems. From Dissipative Structure to Order through Fluctuations. New York, NY: John Wiley & Sons, Inc.; 1977.
2. Koga T, Hashimoto T, Takenaka M, Aizawa K, Amino N, Nakamura M, et al. New insight into hierarchical structures of carbon black dispersed in polymer matrices: a combined small-angle scattering study. Macromolecules. 2008;41:453–64.
3. Reinforcement of Elastomers. In: Kraus, G., editor. New York: Interscience; 1965.
4. Koenig JL. The chemical reactions of network structures in elastomers. Acc Chem Res. 1999;32:1–8.
5. Babu RR, Naskar K. Advanced rubber composites. In: Heinrich, G, editor. Springer-Verlag, Berlin; 2011. p. 219–48.
6. Yamaguchi D, Yuasa T, Sone T, Tominaga T, Noda Y, Koizumi S, et al. Hierarchically self-organized dissipative structures of filler particles in poly(styrene-ran-butadiene) rubbers. Macromolecules. 2017;50:7739–59.
7. Botti A, Pyckhout-Hintzen W, Richter D, Urban V, Straube E. A microscopic look at the reinforcement of silica-filled rubbers. J Chem Phys. 2006;124:174908-1-5.
8. Tsutsumi F, Sakakibara M, Ohshima N. Structure and dynamic properties of solution SBR coupled with tin compounds. Rubber Chem Technol. 1990;63:8–22.
9. Aizawa K, Tomimitsu H. Design and use of a double crystal diffractometer for very small angle neutron scattering at JRR-3M. Physica B. 1995;213:884–6.
10. Koga T, Hart M, Hashimoto T. Development of a high-flux- and high-temperature-set-up bonse-hart ultra-small-angle x-ray scattering (USAXS) diffractometer. J Appl Cryst. 1996;29:318–24.
11. Hart M, Koga T, Takano Y. Mixing symmetric and oblique Bragg reflections in rigid channel-cut crystals. J Appl Cryst. 1995;28:568–70.
12. Rathje J, Ruland W. Density fluctuations in amorphous and semicrystalline polymers. Colloid Polym Sci. 1976;254:358–70.
13. Hendricks RW. A unified theory of absolute intensity measurements in small-angle X-ray scattering. J Appl Cryst. 1972;5:315–24.
14. Hashimoto T, Tanaka H, Koizumi S, Naka K, Chujo Y. A combined small-angle scattering study of a chemical reaction at specific sites and reaction-induced self-assembly as a problem in open non-equilibrium phenomena. J Appl Cryst. 2007;40:s73–7.
15. Freltoft T, Kjems J, Sinha SK. Power-law correlations and finite-size effects in silica particle aggregates studied by small-angle neutron scattering. Phys Rev B. 1986;33:269–75.
16. Gerspacher M, O'Farrell CP. Carbon black is a fractal object. An advanced look at an important filler. Elastomerics. 1991;123:35–9.
17. Schmidt PW. Small-angle scattering studies of disordered, porous and fractal systems. J Appl Cryst. 1991;24:414–34.
18. Rieker TP, Hindermann-Bischoff M, Ehrburger-Dolle F. Small-angle X-ray scattering study of the morphology of carbon black mass fractal aggregates in polymeric composites. Langumuir. 2000;16:5588–92.
19. Guinier A, Fournet G. Small-Angle Scattering of X Rays. London: Wiley; 1955.
20. Beaucage G. Approximations leading to a unified exponential/power-law approach to small-angle scattering. J Appl Cryst. 1995;28:717–28.
21. Hashimoto T. Principles and Applications of X-ray, Light and Neutron Scattering. Tokyo, Japan: Japanese book, Kodannsha Scientific, Inc.; 2017.
22. Hashimoto T. “Mechanics” of molecular assembly: real-time and in-situ analysis of nano-to-mesoscopic scale hierarchical structures and nonequilibrium phenomena. Bull Chem Soc Jpn. 2005;78:1–39.
23. Hashimoto T. Light scattering from multicomponent polymer systems in shear fields: real-time, in situ studies of dissipative structures in open nonequilibrium systems. In: “Soft Matter Characterization”, Borsali R, Pecora R, editors. New York, NY: Springer; 2008. p. 373–462. Vol. 1, Chapter 8.

24. Watson WF. Combination of rubber and carbon black on cold milling. Ind Eng Chem. 1955;47:1281–6.
25. Stickney PG, Faub RD. Carbon black-rubber interactions and bound rubber. Rubber Chem Technol. 1964;37:1299–340.
26. Gessler AM. Evidence for chemical interaction in carbon and polymer associations. butyl and acidic oxy blacks. The possible role of carboxylic acid groups on the black. Rubber Chem Technol. 1969;42:850–57.

Takeji Hashimoto received degrees from Kyoto University (BS, 1965 and MS, 1967) and from the University of Massachusetts (PhD, 1971). He was appointed as an Assistant Professor in 1971 in the Faculty of Engineering, Kyoto University and was promoted to full Professor in 1994. He was a director of the Hashimoto Polymer Phasing Project, ERATO, JST from 1993 to 1998. He had been appointed as a group leader for the Project, "Neutron Scattering and Structure-Functionality of Soft Matters" at Advanced Science Research Center (ASRC), JAEA from 2003 to 2005. Since his retirement at Kyoto University, 2005, he has been Professor Emeritus of Kyoto University and was appointed as a full-time researcher at ASRC, JAEA (2005–2008) as a group leader. He had been a Visiting Scientist at JAEA (2008–2015), a Visiting Professor at School of Science and Technology, Kwanseigakuin University, Hyogo (2008–2011), and an Honorary Chair Professor, National Tsing Hua University, Taiwan (2011–2016) and at National Chenkung University, Taiwan (2017 to present). His research interests include "polymer phasing", viz., elucidation of mechanisms and dynamics of self-organization of molecular assemblies in multicomponent polymer systems (block copolymers, polymer blends, etc.) via phase transitions and phase separation without and with externally applied fields.

Naoya Amino is the General Manager of Amino laboratory in Yokohama Rubber Co., Ltd. (YRC). In 1993 he graduated from the faculty of engineering, department of polymer chemistry, Kyoto University. Then he entered the Yokohama Rubber Co., Ltd. From 1998 he studied on friction mechanisms of silica filled- and carbon black filled-rubbers in Kanazawa University. Then he obtained his doctoral degree in 2001. He is researching and developing new rubber compounding technologies.

Shotaro Nishitsuji was born in Japan in 1980. He received his Bachelor's (2004), Master's (2006), and PhD (2009) degree in Engineering at Kyoto University. He was a project assistant professor at Yamagata University for 3 years from April 2009. Beginning in April 2012, he became an assistant professor at Yamagata University. His current research focuses on the change of filler dispersion in rubber under deformation by using X-ray scattering.

Mikihito Takenaka is currently a Professor of Institute for Chemical Research in Kyoto University. He received degrees from the Kyoto University (the master's degree of engineering in 1988 and the doctor's degree of engineering in 1993 with Professor Takeji Hashimoto). Then, he joined the group of Professor Benjamin Chu, the State University of New York at Stony Brook, USA as a postdoctral fellow from 1993 to 1995. From 1995 to 1997, He joined Hashimoto Polymer Phasing project, ERATO, as a postdoctral fellow. In 1997 He was appointed as an Assistant Professor of Department of Polymer Chemistry in Kyoto University, and was promoted to Professor of Institute for Chemical Research in 2016. His research scope includes the dynamics of phase transitions of polymer alloys, the hierarchical structures of soft matter, the viscoelastic effects of polymeric materials, and the directed self-assembling of block copolymer thin films towards nanopatterning.